Dalton
Transactions

PAPER

View Article Online
View Journal | View Issue

Cite this: *Dalton Trans.*, 2024, **53**, 16241

Trivial positional isomerism in ligands triggering different properties in Fe(II)-metallopolymers; design, synthesis, and characterization†

Shubham Bawa,[a] Anil Kumar,[a,b] Gaurav Kumar Nim,[c] Jayanta Bera,[d] Samaresh Ghosh,[a] Satyajit Sahu,[d] Prasenjit Kar[c] and Anasuya Bandyopadhyay*[a]

The tunable molecular scaffold of organic moieties in metallopolymers generates variation in their properties, but what could be the minimal change that can produce variation in the properties of these macromolecules is still untouched. This research has meticulously explored the trivial change in the molecular scaffold of the ligand capable of making a mammoth difference in the nonvolatile memory and coordination pattern in two metallopolymers. The significance of this research lies in the fact that it demonstrates how a slight change in the organic building block can significantly alter the memristive and fluorescence properties of iron(II) metallopolymers, opening up new possibilities for their design and synthesis. Two novel positional isomeric ligands and their corresponding iron(II)-polymers were synthesized and thoroughly characterized using NMR, XRD, ATR-IR, FESEM, AFM and other techniques. Bright orange solid and solution state fluorescence was observed both in the solid and solution states for ligand $\mathbf{L_2}$ (3,3′-bis((*E*)-(pyridin-3-ylimino)methyl)-[1,1′-biphenyl]-4,4′-diol), while ligand $\mathbf{L_1}$ (3,3′-bis((*E*)-(pyridin-2-ylimino)methyl)-[1,1′-biphenyl]-4,4′-diol) showed blue fluorescence in the solution state only. A robust memristive property for Fe(II)-$\mathbf{L_1}$-poly with a high current ON/OFF ratio of 10^4, remarkable random access behaviour, and a long retention time greater than 35 000 seconds was observed while its counterpart was entirely silent. Both polymers showed solution-state electrochromism. These synthesised metallopolymers also showed good specific capacitance in the range of 50–60 F g^{-1} with a remarkable retention of 98% of the initial value even after 5000 charge–discharge cycles. The AFM and FESEM micrographs revealed the formation of long polymer nano-rods, which correlates with the NMR, ATR-IR, and XRD results. The difference in the properties of polymers generated by such a slight change in the organic building block forces different coordination patterns of these two ligands around the same central metal ion, and this is also evident in all the characterization methods.

Received 30th July 2024,
Accepted 12th September 2024

DOI: 10.1039/d4dt02175d

rsc.li/dalton

Introduction

In the diverse field of hybrid materials, metallopolymers are one branch that has attracted the attention of different research groups worldwide. Their attention is due to the variable properties shown by these metallopolymers.[1–3] The coordination of multidentate ditopic organic moieties with different metal ions, such as transition metal ions, lanthanides, and the main group metal ions, forms the metallopolymers through the complexation reaction. This metal–ligand coordination generates various beneficial and easily tunable properties (optical, magnetic, electrochemical, *etc.*) in these polymers because of the redistribution of the energy levels of the ligand and the central metal ion[4,5] after complexation. A repetitive pattern of the same coordination sphere upon coordination will generate a long 1D chain of metallopolymers. They can be used as smart functional materials such as thermochromic,[6–8] solvatochromic,[9] electrochromic,[10–14] chemosensor,[15,16] and nonvolatile memristive materials[17–20] and sensors,[21] which can respond to external stimuli like temperature, solvents, potential, and chemical exposure, as well as an electrode in a supercapacitor, and energy storage devices.[22] Their properties can be modulated by either tuning the coordination sites of organic moieties, varying the conjugation length in the

---

[a] Department of Polymer & Process Engineering, IIT Roorkee, Saharanpur Campus, Saharanpur-247001, India. E-mail: anasuya.bandyopadhyay@pe.iitr.ac.in
[b] Department of Food & Nutrition, Kunsan National University, Gunsan-54150, South Korea
[c] Department of Chemistry, IIT Roorkee, Roorkee-247667, India
[d] Department of Physics, IIT Jodhpur, Rajasthan-342037, India

† Electronic supplementary information (ESI) available. See DOI: **https://doi.org/10.1039/d4dt02175d**

organic counterpart, imparting structural variation such as flexibility/rigidity,[15] changing the chelating ring size of binding organic moieties, or combining with different metal ions.[23–28] The crux of the discussion is that the structural tunability of the organic moiety combined with various metal ions is responsible for a broad range of properties generated by these metallopolymers. These changes, in any way, would ultimately produce a difference in the energy level of the highest occupied molecular orbital (HOMO) and lowest unoccupied molecular orbital (LUMO) states.

In this research article, we have designed and synthesised two organic moieties bearing the same coordination sites to synthesise two Fe(II)-metallopolymers. These two newly developed ligands have trivial positional isomerism. Much literature has focused on tuning different properties such as smart coatings, self-healing materials, shape-memory materials,[29] photovoltaic materials, sensing materials,[30] and electrochromic[31] and supercapacitor materials[32] by tailoring different ligands. Our aim during the design of ligands was to explore the effect of positional isomerism on the coordination behaviour with the same central metal ion. Positional isomerism in ligands will vary the size of chelating rings upon coordination, which will play a role in the evolution and stabilisation of the several properties of metallopolymers. This would also expose one new aspect of the structure–property relationship, which is still untouched. The complexation reaction of these newly synthesised ligands with Fe(II)–metal salts produces two different metallo-supramolecular polymers, which have been thoroughly investigated with various analytical techniques to understand their structure–property relationship.

Experimental section

Materials

4,4′-Dihydroxybiphenyl and anhydrous $FeCl_2$ were purchased from Sigma-Aldrich, India Pvt. Ltd and used as they were. 2-Amino pyridine and 3-amino pyridine were purchased from TCI Chemicals India Ltd. Tetraethyl orthosilicate and tetrabutylammonium perchlorate (TBAP) were purchased from TCI Chemicals India Ltd. Trifluoroacetic acid (CF_3COOH) and hexamethylenetetramine (HMTA) were purchased from Sigma-Aldrich, India Pvt. Ltd. Calcium hydride and sodium metal were purchased from LOBA (India). Sodium bicarbonate and hydrochloric acid (HCl) were purchased from HiMedia India Ltd. DCM and ethanol were obtained from Merck India Ltd. The solvents used were AR grade and purified by standard procedures before use. All solvents used for characterization studies were HPLC grade and purchased from Merck, India.

Caution: The acids used harm health and may cause injury; they should be used with proper precautions.

Instrumentation and characterization

All samples' NMR spectra (^1H and ^{13}C) were measured using a Bruker 500 Hz spectrometer with tetramethylsilane (TMS) as a reference. The ATR-IR (attenuated total reflectance infra-red) spectra of all samples were recorded in the range of 4000–500 cm^{-1} on a PerkinElmer FT-IR C91158 spectrophotometer having a zinc selenide crystal. The wide-angle X-ray diffraction (WXRD) patterns of the sample were collected in the angle range of 2θ = 5–80° at a scan rate of 4° min^{-1} using a RIGAKU ULTIMA IV X-ray diffractometer, with Ni filtered Cu Kα as a radiation source. The UV experiments were done on a Shimadzu UV spectrophotometer (UV-Vis 1800). A CH instrument (CH1620D) was used for cyclic voltammetry (CV) measurements at a 100 mV s^{-1} scan rate. Atomic force microscopy (AFM) imaging of the polymer was carried out on a freshly cleaved highly ordered pyrolytic graphene (HOPG) substrate using an NT-MDT-INTEGRA microscope in the tapping mode at room temperature. Field emission scanning electron microscopy (FESEM) images of the sample were recorded on a TESCAN MIRA 3 microscope by pouring a 10^{-5} M sample solution on glass slides followed by air and vacuum drying. The polymer-coated glass slide of 1 cm^2 was then mounted on stubs and sputtered with gold using a vacuum sputter. Thermal analysis of metallopolymers (roughly 10 mg) was done by thermogravimetric analysis (TGA) with a TA Instruments TGA55 Discovery series instrument under an N_2 atmosphere. The temperature was increased from 30 to 800 °C with a sweep rate of 10 °C min^{-1}. The DSC experiment was done with a TA Instruments DSC 25 Discovery series instrument to find the T_g and T_m of the polymeric samples. A series of heating/cooling/heating (150 °C/30 °C/150 °C) cycles was performed to remove the background inaccuracy. A digital melting point apparatus was used to determine the melting point of the two ligands and other small molecules. A Brookhaven BI-200SM goniometer was used for absolute molecular weight determination of the metallopolymers. An EUTECH Instruments CON 700 was used for conductivity measurements. A Keithley 6430 femto-ampere source meter was used for electrical characterization using two probe measurement techniques.

Device fabrication

***i–V* study.** The ITO was etched using zinc dust and hydrochloric acid to form a sharp ITO (bottom electrode) strip on the ITO-coated glass substrate. The etched substrates were cleaned in acetone, DI water, and methanol for 15 min each in an ultra-sonication bath and dried with an N_2 gun. Fe(II)-**L₁**-poly was then dissolved in a mixture of methanol and DMSO with a volume ratio of 1 : 9. The polymer solution concentration was kept at 20 mg ml^{-1} for spin coating. This solution was then spin-coated at 2500 rpm for 40 seconds, and then heated at 70 °C on a hotplate for 30 minutes. A shadow mask was then used to deposit a 130 nm thick aluminium layer using a thermal deposition system at a base pressure of 5.2×10^{-6} Torr for the top electrode deposition. The active area of each cell was 1 mm^2. The schematic of the device structure is shown in Fig. 12a. The same procedure was followed for device fabrication with each ligand and Fe(II)-**L₂**-poly.

Capacitance studies. The capacitance studies were performed using a three-electrode system by drop-casting the active material on 3 mm diameter GC as the working electrode, Ag/AgCl as the reference electrode, and a Pt wire as the counter electrode in 1 M LiCl aqueous electrolyte solution. The working electrode was prepared using the drop-casting technique. After dissolving a certain amount of metallopolymer in the DMSO solvent, a specific volume of that solution was drop-casted on GC, followed by drying in an oven under vacuum for more than 24 h.

Synthesis of ligands

Synthesis of 4,4′-dihydroxy-[1,1′-biphenyl]-3,3′-dicarbaldehyde (1)

Duff's formylation. The synthesis of the dicarbaldehyde derivative of 4,4′-dihydroxybiphenyl was done by following a simple route of Duff's formylation reaction.[33] 4,4′-Dihydroxybiphenyl (1.86 g, 10 mmol) and HMTA (2.10 g, 15 mmol) were dissolved in CF_3COOH (30 ml) under N_2 and stirred for 4 h at 120 °C. The solution was then brought to room temperature and poured into 4 N HCl (400 ml) and stirred for 12 h. The product was filtered, and a solid yellow mass was collected. The collected precipitate was thoroughly washed with water and dried under vacuum. The crude mass was purified using the dry silica column chromatography technique using DCM as an eluent to get the pure compound. Yield: 1.62 g (67%). M.P.: 231 °C; ^{1}H NMR (500 MHz, DMSO-d$_6$): δ (ppm) 10.85 (s, 2H), 10.32 (s, 2H), 7.89 (d, 2H) $J \sim 3$ Hz, 7.82 (dd, 2H) $J_1 \sim 3$ Hz, $J_2 \sim 10.5$ Hz, 7.09 ppm (d, 2H) $J \sim 10.2$ Hz. ATR-IR (cm^{-1}): 3435, 2925, 2866, 1663, 1590, 1474, 1374, 1281, 1235, 1187, 884, 834, 771, 737, 693, 567, 463.

Synthesis of 3,3′-bis((*E*)-(pyridin-2-ylimino)methyl)-[1,1′-biphenyl]-4,4′-diol (ligand L$_1$). 4,4′-Dihydroxy-[1,1′-biphenyl]-3,3′-dicarbaldehyde (242 mg, 1 mmol) and 2-aminopyridine (189 mg, 2 mmol) were dissolved in absolute ethanol in the presence of tetraethyl orthosilicate in a three-neck round bottom flask under an N_2 atmosphere and refluxed at 85 °C for 48 h (Scheme 1). The coupling product was obtained as brick red colour precipitates in the reaction mixture. The TLC method was employed to monitor the reaction progress. After completion of the reaction, the mixture was cooled and then filtered. The precipitates obtained were washed with 30% methanol and purified by recrystallisation in methanol. Yield: 308 mg (78%). M.P.: 260 °C; ATR-IR (cm^{-1}): 3428, 3057, 1613, 1553, 1462, 1429, 1280, 1181, 1137, 902, 804, 706, 630, 556; ^{1}H NMR (500 MHz, DMSO-d$_6$) δ (ppm) 13.10 (s, 2H), 9.61 (s, 2H), 8.59 (dd, 2H) $J_1 \sim 2$ Hz, $J_2 \sim 6$ Hz, 8.19 (d, 2H) $J \sim 3$ Hz, 7.98 (td, 2H) $J_1 \sim 3.5$ Hz, $J_2 \sim 9$ Hz, 7.81 (dd, 2H) $J_1 \sim 2.5$ Hz, $J_2 \sim 1.5$ Hz, 7.52 (d, 2H) $J \sim 6$ Hz, 7.40 (dd, 2H) $J_1 \sim 5.5$ Hz, $J_2 \sim 13$ Hz, 7.11 (d, 2H) $J \sim 6$ Hz.

^{13}C NMR (125 MHz, $CDCl_3$) δ (ppm) 118.7, 119.0, 119.5, 120.9, 131.4, 132.8, 134.3, 137.3, 145.0, 156.8, 160.0, 161.8 (Fig. S1†). Elemental anal. calcd for $C_{24}H_{18}N_4O_2$: C, 73.09; H, 4.59; N, 14.20. Found: C, 72.99; H, 4.52; N, 14.17; $C_{24}H_{18}N_4O_2$; ESI-MS: *m*/*z* calcd: 394.590; found: 395.144 (Fig. S2†).

Synthesis of 3,3′-bis((*E*)-(pyridin-3-ylimino)methyl)-[1,1′-biphenyl]-4,4′-diol (ligand L$_2$). Ligand **L$_2$** was synthesized in a similar manner to that of ligand **L$_1$** with the only difference of using 3-aminopyridine instead of 2-aminopyridine. The precipitates obtained were washed with 30% methanol and purified by recrystallization in methanol (Scheme 1). Yield: 330 mg

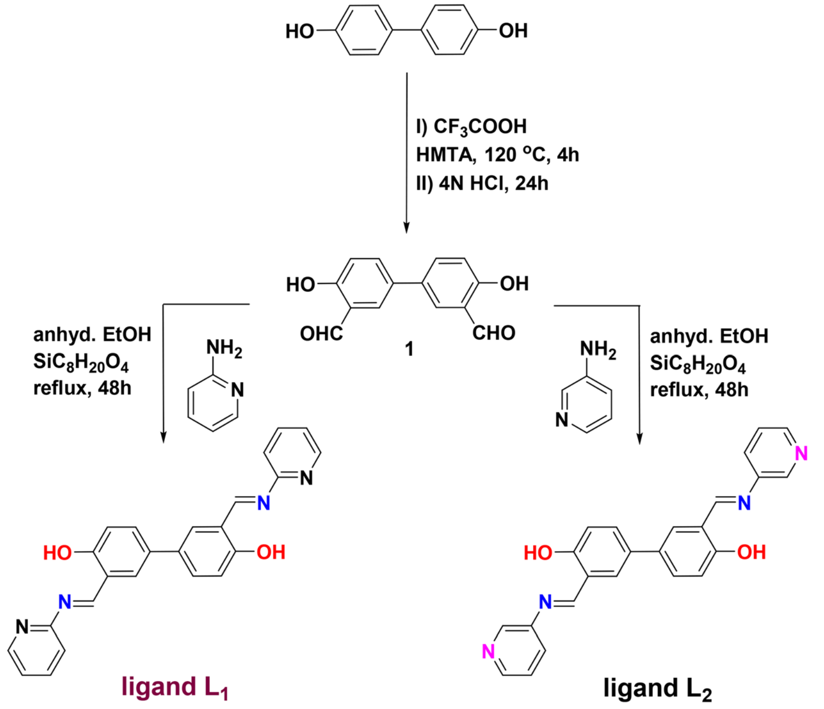

Scheme 1 Syntheses of ligands L$_1$ and L$_2$.

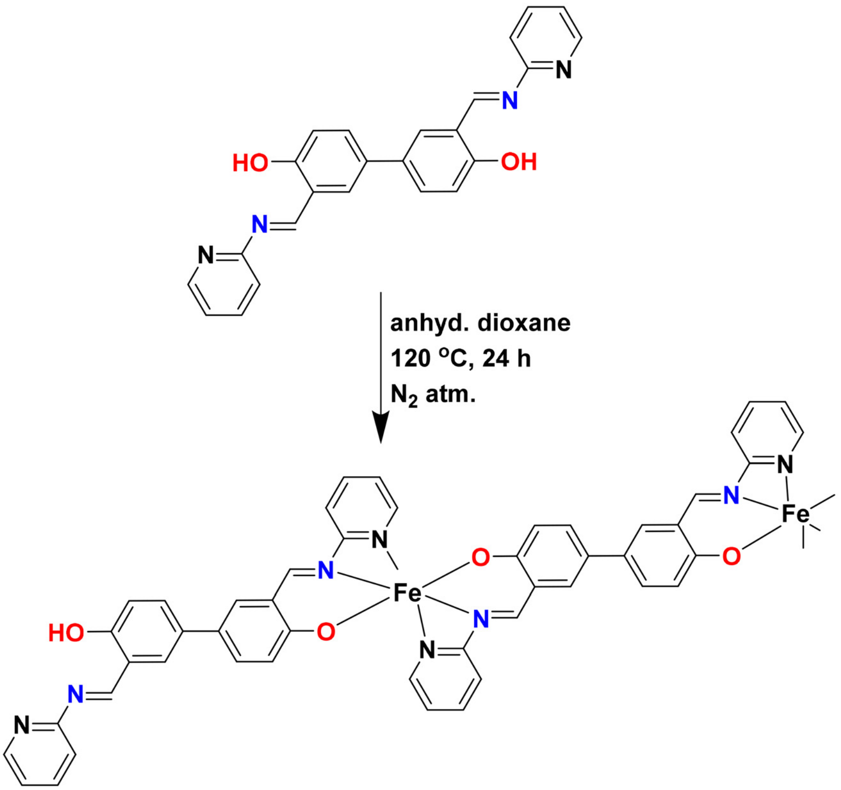

Scheme 2 Schematic representation of the possible Fe(II)-**L**$_1$-poly structure.

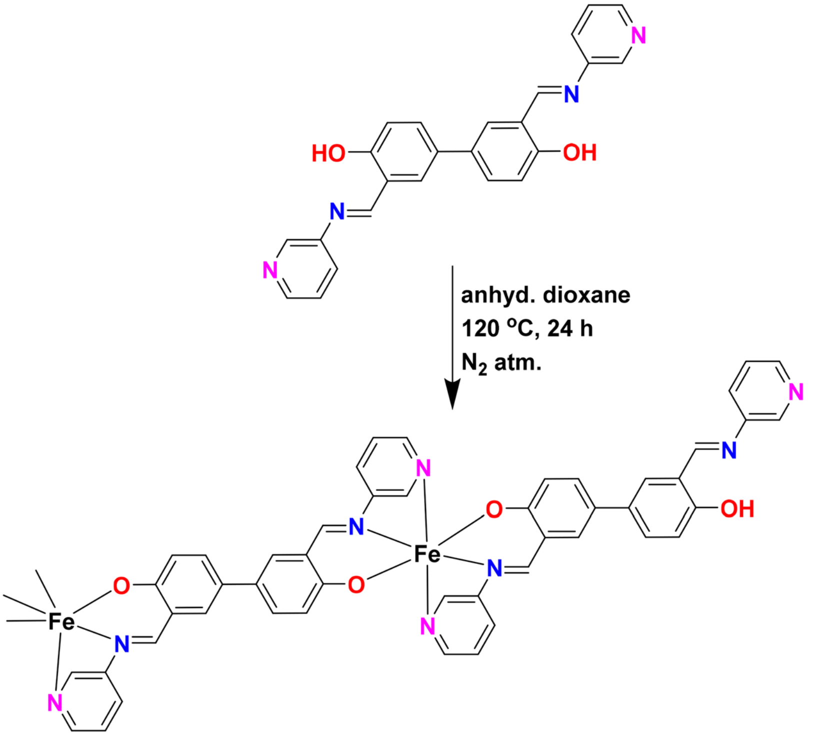

Scheme 3 Schematic representation of the possible Fe(II)-**L**$_2$-poly structure.

(84%). M.P.: 267 °C; ATR-IR (cm^{-1}): 3405, 2876, 1592, 1531, 1439, 1319, 1243, 1153, 1084, 865, 767, 669, 577, 524; ^1H NMR (500 MHz, DMSO-d_6) δ (ppm) 12.52 (s, 2H), 9.12 (s, 2H), 8.66 (d, 2H) J 3 Hz, 8.53 (d, 2H) $J \sim 4.2$ Hz, 8.04 (d, 2H) $J \sim 2.4$ Hz, 7.88 (dd, 2H) $J_1 \sim 3$ Hz, $J_2 \sim 10.2$ Hz, 7.77 (dd, 2H) $J_1 \sim 3$ Hz, $J_2 \sim 10.2$ Hz, 7.53 (dd, 2H) $J_1 \sim 5.5$ Hz, $J_2 \sim 4$ Hz, 7.10 (d, 2H) $J \sim 10.2$ Hz.

^{13}C NMR (125 MHz, $CDCl_3$) δ (ppm) 119.0, 121.9, 123.8, 127.3, 131.41, 132.81, 142.5, 143.6, 148.1, 160.0, 160.0 (Fig. S3†). Elemental anal. calcd for $C_{24}H_{18}N_4O_2$: C, 73.09; H, 4.59; N, 14.20. Found: C, 73.01; H, 4.50; N, 14.18; $C_{24}H_{18}N_4O_2$; ESI-MS: *m*/*z* calcd 394.590; found: 395.144 (Fig. S4†).

Synthesis of Fe(II)-L_1-poly. For Fe(II)-**L_1**-poly, 100 mg (0.25 mmol) of ligand **L_1** was dissolved in 300 ml of dioxane, followed by the addition of 72 μl (0.50 mmol) of triethylamine (TEA) to deprotonate the –OH group of the ligand. The mixture was stirred for 10 minutes, and 32.04 mg (0.25 mmol) of $FeCl_2$ was added and refluxed under a nitrogen atmosphere for 24 h. The TLC method was employed to monitor the reaction progress from time to time. The reaction was stopped and cooled down when the TLC process indicated complete ligand consumption. It was then filtered with a cotton plug. The filtrate was evaporated entirely in a Petri dish to obtain a solid mass that was further purified by the rapid precipitation method to remove the unreacted ligand and oligomer. Yield: 92.43 mg (69%), T_m = 265 °C, T_c = 210 °C, T_g = 140 °C (Fig. S7†). ATR-IR (cm^{-1}): 2940, 1602, 1470, 1456, 1432, 1288, 1167, 828, 706, 608, 548. ^1H NMR (500 MHz, DMSO-d_6) δ (ppm) 10.32 (br, 2H), 8.67 (br, 2H), 8.36 (br, 2H), 7.91 (br, 2H), 7.78 (br, 2H), 7.62 (br, 2H), 7.42 (br, 2H), 7.10 (br, 2H). The absolute molecular weight of the polymer was found to be $(3.72 \pm 0.8) \times 10^4$ g mol^{-1} using the SLS technique *vide* Fig. S6† (degree of polymerization (n) = approx. 107) (Scheme 2).

Synthesis of Fe(II)-L_2-poly. Fe(II)-**L_2**-poly was synthesised by the same process as that discussed for Fe(II)-**L_1**-poly with 100 mg (0.25 mmol) of ligand **L_2** and 32.04 mg (0.25 mmol) of $FeCl_2$. Yield: 81.40 mg (62%), T_m = 280 °C, T_c = 230 °C, T_g = 125 °C (Fig. S9†). ATR-IR (cm^{-1}): 2974, 1583, 1566, 1444, 1405, 1377, 1268, 1137, 786, 672, 573. ^1H NMR (500 MHz, DMSO-d_6) δ (ppm) 9.14 (br, 2H), 8.78 (br, 2H), 8.64 (br, 2H), 8.11 (br, 2H), 7.78 (br, 2H), 7.90 (br, 2H), 7.78 (br, 2H), 7.08 (br, 2H). The absolute molecular weight of the polymer was found to be $(4.04 \pm 0.8) \times 10^4$ g mol^{-1} using the SLS technique (Fig. S8†) (degree of polymerization (n) = 87) (Scheme 3).

Results and discussion

The driving force of this research is to explore the modulation effect of the size of the chelating ring of the ligands on conjugated metallopolymers' properties. We have designed and synthesised two novel multidentate, ditopic organic ligands possessing N, N, and O/OH as binding sites on each coordination half. Ligand **L_1** and ligand **L_2** were synthesised by Schiff's base coupling reaction of formyl compound **1** with 2-aminopyridine and 3-aminopyridine, respectively. They were allowed to react with the $FeCl_2$ salt in a 1 : 1 proportion under identical conditions to form two different type-II metallopolymers. As these ligands are positional isomers, we expect a variation in the chelate ring size upon coordination. Ligand **L_1** is supposed to create six-membered and four-membered chelating rings, while its positional isomer (**L_2**) forms six-membered and five-membered chelating rings when coordinated to the Fe(II) metal ion.

In the case of ligand **L_2**, as the 3-amino pyridine coordination site is further away from the imine bond by a distance of 1C atom compared to that of 2-amino pyridine in ligand **L_1**, there is a possibility that all three coordination sites (N, N, and O) of one face of this ditopic ligand may not bind to the same metal ions. There could be a different coordination pattern, as shown in Scheme 4 for ligand **L_2**. The ^1H NMR spectrum and ATR-IR and XPS spectra will be conclusive in getting insight into the coordination pattern of ligand **L_2**.

It is clear from coordination pattern-II that steric hindrance will be very high if another one/two ligand(s) coordinate(s) to the same metal centre from the top and bottom. Another possibility is that a small atom/molecule (X) from the reaction mixture may coordinate to reduce the steric hindrance, which XPS, ATR-IR, NMR, and other characterization studies can confirm. However, in that case, the pyridine N will remain uncoordinated. If we consider the ligand field strength of the three coordination sites in our ligand, then $N_{py} > N_{imine} > O^-$, so the pyridine N will coordinate first, bringing the other two coordination sites close, becoming a tridentate chelate. However, we need to confirm the actual coordination pattern of ligand **L_2** using different characterization techniques.

ATR-IR studies

The overlaid ATR-IR spectra of ligands **L_1** and **L_2**, along with the respective polymers, are shown in Fig. 1. The analysis of ligand **L_1** shows a band at 3413 cm^{-1} for aromatic –OH stretching and 1592 cm^{-1} and 1523 cm^{-1} bands for –C═N stretching of the free imine bond and the pyridine ring, respectively, while the band at 1439 cm^{-1} was observed for aromatic –C═C stretching. Another band at 1243 cm^{-1} was observed for –C–N stretching. In both polymers, the ATR-IR peak gets broadened, indicating the formation of polymer chains. Similar stretchings for ligand **L_2** were observed with the 3428 cm^{-1} band for aromatic –OH stretching, 1613 cm^{-1} and 1553 cm^{-1} bands for –C═N stretching of the free imine bond and the pyridine ring, respectively, and the 1465 cm^{-1} band for aromatic –C═C stretching. A band at 1280 cm^{-1} was observed for –C–N stretching. Though being positional isomers, almost identical fingerprint regions were observed for the ligands, but distinguished differences were observed upon coordination.

For Fe(II)-**L_1**-poly, the –C═N stretching was observed at 1582 cm^{-1} and 1470 cm^{-1} for the coordinated imine bond and the pyridine ring, and a similar shift was observed for the –C═C stretching at 1456 cm^{-1} and 1432 cm^{-1} while the –C–N stretching got shifted to 1288 cm^{-1}. For Fe(II)-**L_2**-poly, the –C═N stretching was observed at 1602 cm^{-1}, while at

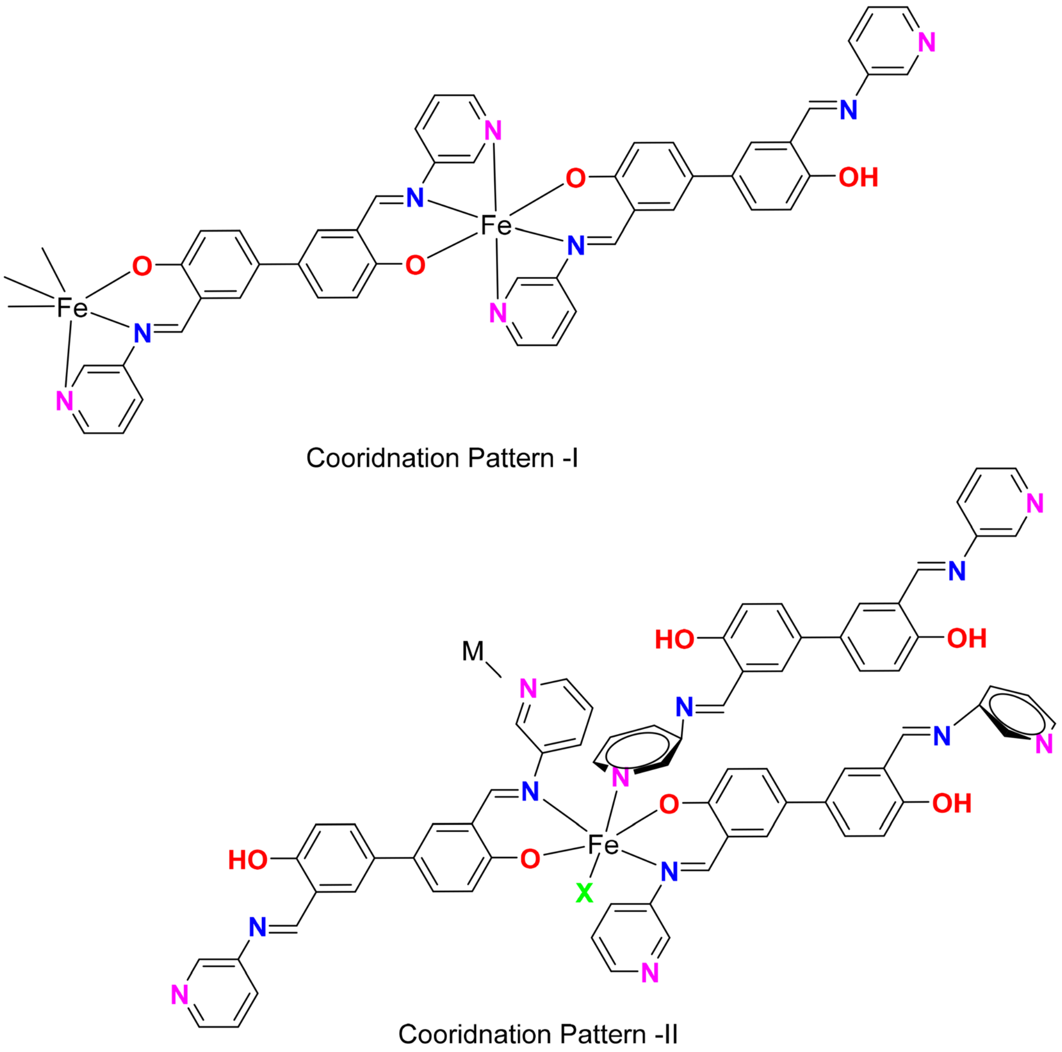

Scheme 4 Coordination patterns for the Fe(II)-L_2-poly structure.

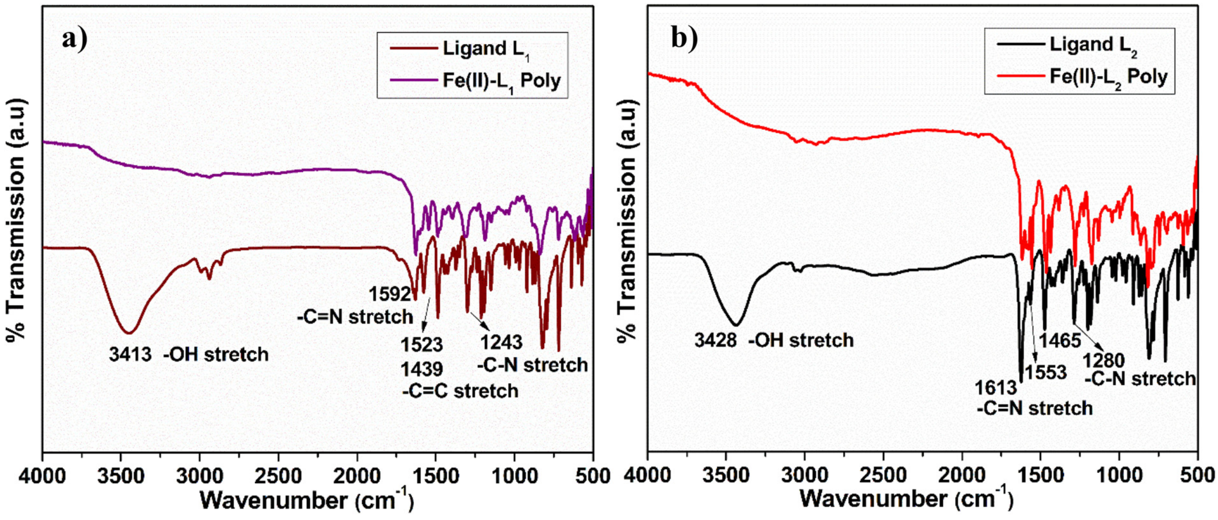

Fig. 1 (a) Overlaid ATR-IR spectra of ligand $\mathbf{L_1}$ and Fe(II)-$\mathbf{L_1}$-poly and (b) ligand $\mathbf{L_2}$ and Fe(II)-$\mathbf{L_2}$-poly.

1470 cm^{-1}, a peak was observed for the pyridine ring. The –C═C stretchings were found at 1444 cm^{-1} and 1405 cm^{-1}, while the –C–N stretching was shifted to 1377 cm^{-1}. A broad hump nearly in the 3500–3000 cm^{-1} range was observed in the case of Fe(II)-$\mathbf{L_2}$-poly, which indicates that all of the hydroxyl groups may not be deprotonated, and there is a possibility of the presence of an –OH neutral donor group instead of an –O^{-1} anionic donor.

NMR studies

The overlaid NMR spectra of both ligands and their respective Fe(II)-metallopolymers are shown in Fig. 2. As both ligands have symmetric structures, only one-half of the ligand was responsive in the NMR spectrum. The ^{1}H NMR spectra of ligand $\mathbf{L_1}$ showed three singlets at 13.10 ppm, 9.61 ppm, and 8.19 ppm, respectively, due to –OH, C-8 (imine H), and C-6 protons. Being *ortho* to an electron-donating hydroxyl group, the C-3 proton experienced maximum shielding and appeared at 7.11 ppm. Similarly, the C-11 proton appeared as a multiplet at 7.40 ppm due to *ortho*, *meta* coupling with C-12 and C-13 protons. Another multiplet was observed at 7.81 ppm for C-13 due to coupling with C-12 and C-14 protons, while a peak for the C-12 proton was observed at 7.98 ppm. Two peaks at 8.59 ppm and 7.52 ppm were observed for C-14 and C-4 protons, respectively. The C-14 proton is close to the electron-withdrawing nitrogen; thus, broadening is observed. The ^{1}H NMR spectra of $\mathbf{L_2}$ showed three singlets at 12.52 ppm, 9.12 ppm, and 8.66 ppm due to –OH, C-8 (imine H), and C-15 protons. The hydroxyl proton and imine-H were shifted upfield compared to ligand $\mathbf{L_1}$ because of the positional shift of the pyridine N. Nevertheless, the C-3 proton appeared at the same position as it is present at the *meta*-position of the imine bond. However, there is a drastic shift in the position of the C-4 and C-6 protons because of their respective *p*- and *o*-positions of the imine bond. The peak of the C-13 proton of the pyridine ring is very feeble and appears at 8.53 ppm. The positional shift of the pyridine N is evident in the shift of the proton signals of C-11, 12, and C-13 protons compared to those of ligand $\mathbf{L_1}$.

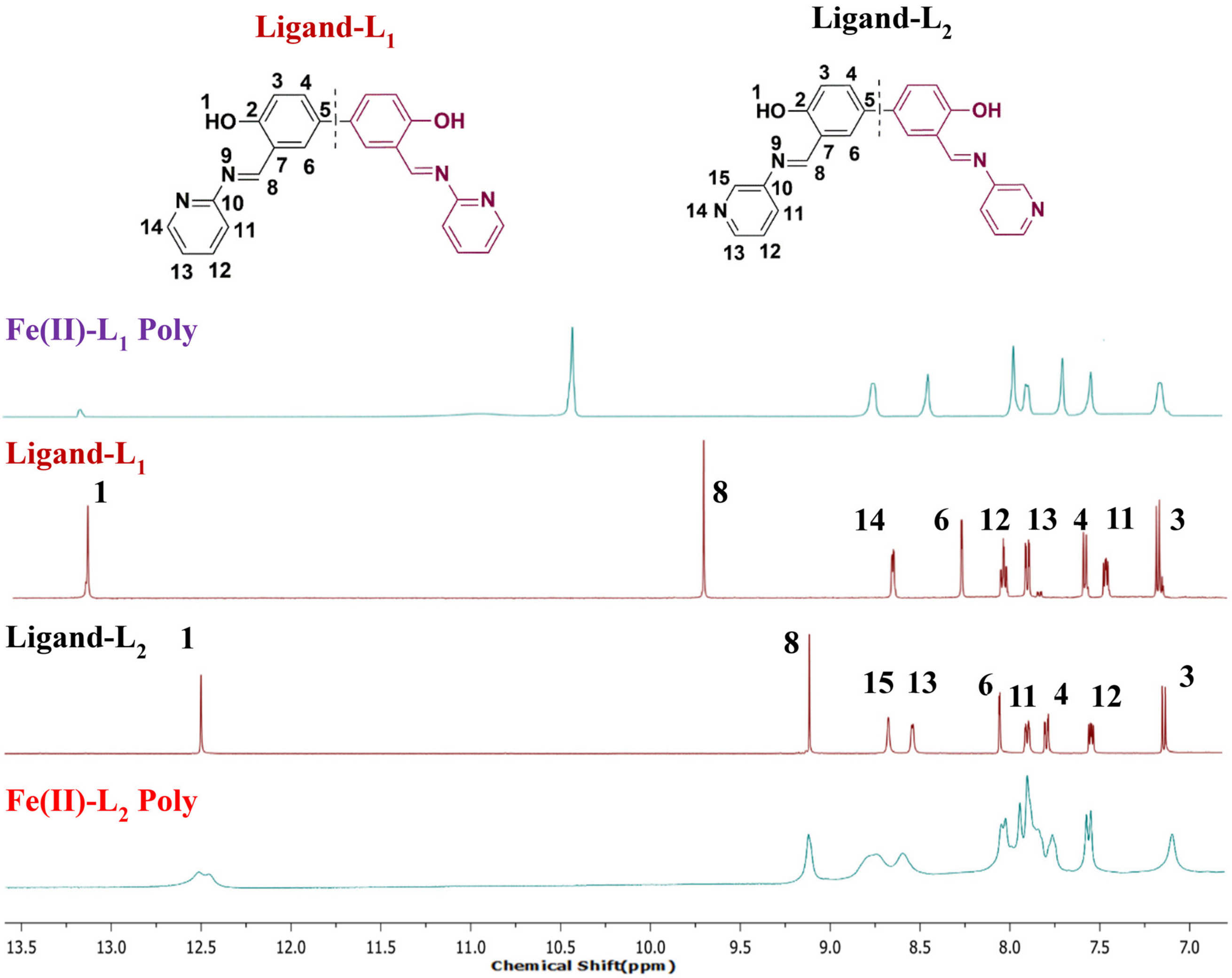

Fig. 2 Overlaid ^{1}H-NMR spectra of both the ligands and their corresponding polymers in DMSO-d$_6$.

In the ^{13}C NMR spectrum of each ligand, 12 peaks (5C from the pyridine group + 6 benzene carbons + 1 imine C) were observed (*vide* Fig. S1 and S3†). Pyridine carbons are most downfield from 135–160 ppm in ligand $\mathbf{L_1}$, while ligand $\mathbf{L_2}$ shows the same between 140 and 160 ppm. The rest of them are upfielded responses of 6 benzene carbons along with one imine carbon in both cases. The characteristic peak of $CDCl_3$ was observed at around 80 ppm in both NMR spectra.

The NMR spectra of both the metallopolymers showed a broadening of proton signals, which is a primary indication of the formation of a polymer molecule.[34–37] The synthesized polymeric materials are not pure molecules but a collection of molecules with identical repeating units but variable chain lengths, causing slight modification in the chemical environment of the protons. Again, polymer molecules in the solution state also have a faster relaxation time than the small organic ligand. These two effects cause a broadening of the NMR spectrum of any polymer molecules in the solution state. In the case of Fe(II)-$\mathbf{L_1}$-poly, the hydroxyl signal has completely vanished, which confirms the coordination of the –OH group in an anionic $–O^{-1}$ fashion. A downfield shift of the imine proton was observed upon coordination with the metal ions due to the donation of the lone pairs of N. A shift of the other protons' positions was also observed due to the complexation reaction. The exact shifting was observed for Fe(II)-$\mathbf{L_2}$-poly. There is a sharp difference in the signal pattern of the NMR spectra of both polymers. A more significant amount of overlapping proton peaks was observed for Fe(II)-$\mathbf{L_2}$-poly at around 8.0 ppm and in the 8.5 to 8.9 ppm range.

The most exciting feature of the ^{1}H NMR spectra of the second polymer is the presence of a small hump of the hydroxyl proton. The ATR-IR spectrum of the corresponding polymer shows O–H stretchings. So, this broad signal at around 12.5 ppm strongly indicates a small amount of –OH in the polymeric chain. Such a hump was absent in the case of Fe(II)-$\mathbf{L_1}$-poly. The very low NMR integration value for the –OH proton was found upon comparison with the imine H peak. This low integration value indicates that after every 8 or 9 $–O^{-}$ binding monomer units, 1 unit possesses the –OH group as a neutral donor. As the hydroxyl group works as a neutral donor when coordinated with a metal ion, it cannot satisfy the primary valency of the metal ion. As a result, the chloride ion is probably present as a counter ion outside the coordination sphere (as shown in Scheme 5) to satisfy the primary valency of a divalent Fe^{2+} ion.

The presence of the Cl^- counter anion was again confirmed by two experiments: a precipitation test with $AgNO_3$ and a conductivity measurement experiment with a series of dilute polymer solutions. The appearance of slight turbidity on adding $AgNO_3$ solution to Fe(II)-$\mathbf{L_2}$-poly solution confirms the presence of Cl^- as a counter anion; however, no turbidity was observed in the case of Fe(II)-$\mathbf{L_1}$-poly (ESI Fig. S16†). This test was also supported by the conductivity measurement experiment with a series of different concentration solutions for both polymers (ESI Table S1†). The result showed conductivity variation for Fe(II)-$\mathbf{L_2}$-poly with a change in the concentration, but the conductivity of Fe(II)-$\mathbf{L_1}$-poly remained unaltered with the concentration change as it is a neutral polymer with no counter anion present outside the coordination sphere. The different coordination pattern after every 8–9 repeating units in Fe(II)-$\mathbf{L_2}$-poly indicates the presence of higher steric strain in the second positional isomer ligand $\mathbf{L_2}$ upon coordination with the same central metal ions.

Its ^{1}H NMR spectrum also confirms the coordination pattern of ligand $\mathbf{L_2}$, as it showed a response for only one-half of the coordinated ligand. If it followed coordination pattern-II, there would be a symmetry withdrawal due to asymmetric coordination, and many more peaks would be observed in the NMR spectrum of the polymer. If the Cl^- ion was present inside the coordination sphere, it was not precipitated in the $AgNO_3$ experiment, which confirms its presence outside the coordination sphere. Solution state conductivity measurements also confirm coordination pattern-I with some hydroxyl groups remaining protonated during coordination with the metal to reduce the difficulty of approaching the metal centre in the proximity required for anionic coordination of hydroxyl oxygen.

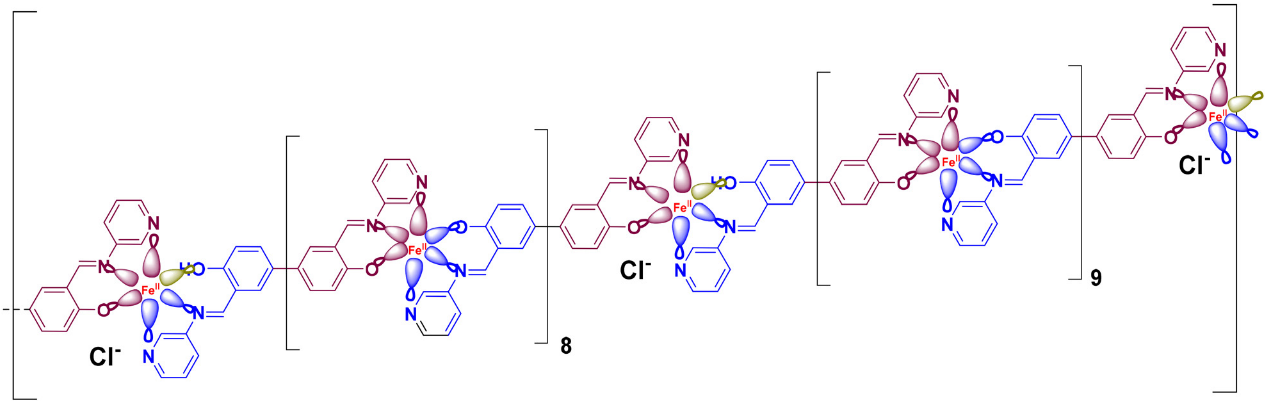

Scheme 5 Representation of the chloride counter anion after every 8–9 monomer units.

XRD studies

XRD studies reveal the extent of crystallinity in the ligands and their corresponding polymers. Fig. 3(a) and (b) are the overlaid XRD images of the ligands and their corresponding metallopolymers. XRD images for both ligands showed sharp peaks, indicating their crystalline nature, as small organic molecules often possess crystallinity. However, the crystallinity gets reduced after the formation of metallopolymers.[38] In the case of Fe(II)-$\mathbf{L_1}$ and Fe(II)-$\mathbf{L_2}$-poly, most of the sharp peaks are either flattened or reduced in intensity, indicating a sharp drop in the crystallinity and enhancement of the amorphous nature in the synthesised polymers and they are semi-crystalline. The long-chain polymers are entangled, and these entangled disordered zones are mainly responsible for creating amorphous regions.[36,37] The XRD analysis confirms that the polymers formed upon the complexation of metals with the respective organic ligands are semi-crystalline.

Study of photophysical properties

The photophysical properties of the ligands and their corresponding Fe(II) polymers were studied using a UV-Vis spectrophotometer. The recorded UV-Vis absorbance spectra are shown in Fig. 4. 10^{-5} M methanolic solutions of ligands $\mathbf{L_1}$ and $\mathbf{L_2}$ and the corresponding Fe(II) polymers were prepared,

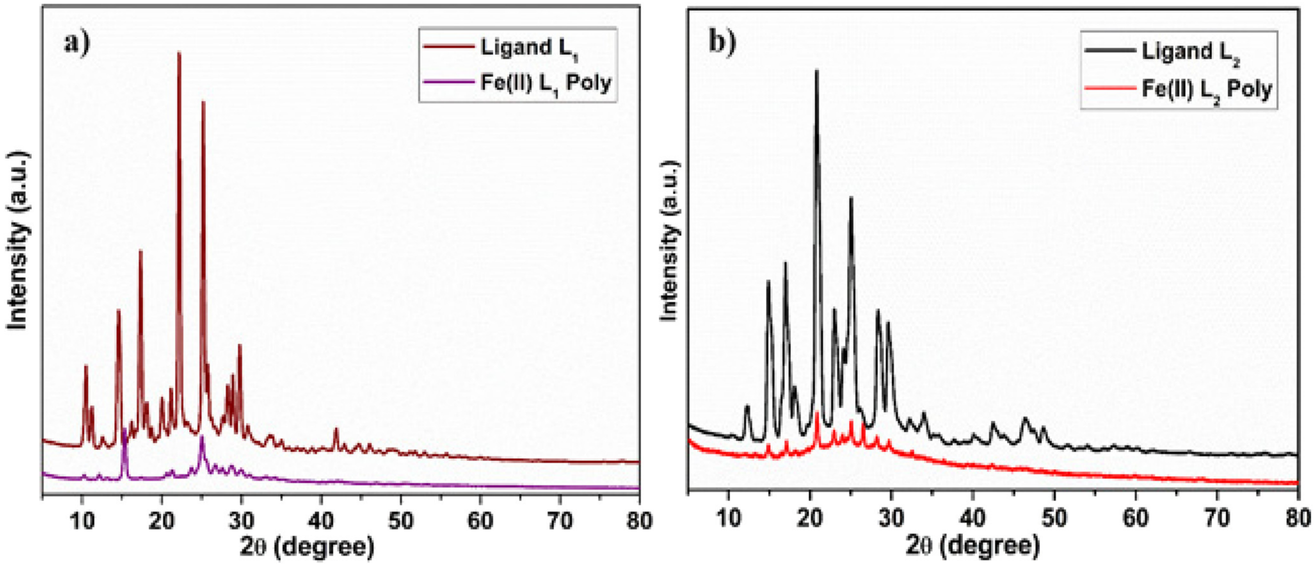

Fig. 3 XRD graph of (a) ligand $\mathbf{L_1}$ and Fe(II)-$\mathbf{L_1}$-poly and (b) ligand $\mathbf{L_2}$ and Fe(II)-**L2**-poly.

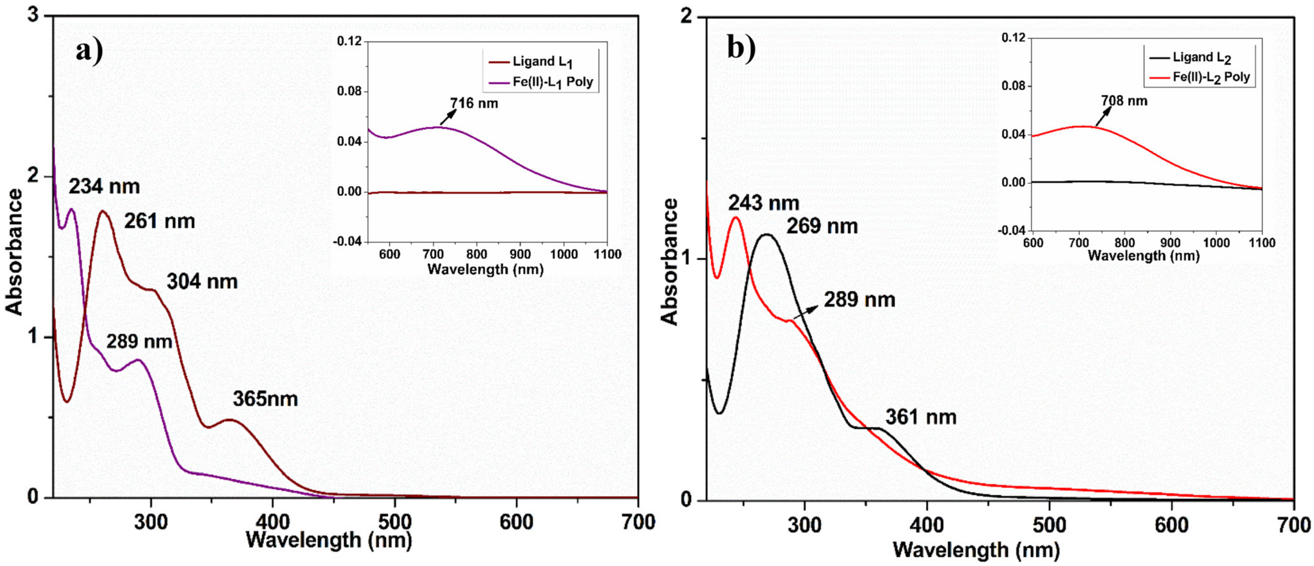

Fig. 4 (a) UV-Vis spectra of 10^{-5} M methanolic solution of ligand $\mathbf{L_1}$ and Fe(II)-$\mathbf{L_1}$-poly (inset shows d–d transition) and (b) UV-Vis spectra of 10^{-5} M methanolic solution of ligand $\mathbf{L_2}$ and Fe(II)-$\mathbf{L_2}$-poly (inset shows d–d transition).

and their spectra were recorded. The UV-absorbance spectra of ligand $\mathbf{L_1}$ showed three absorbance bands at 365, 304, and 261 nm, respectively.

The band at 365 nm was assigned to n–π* transitions generated from lone pairs of heteroatoms. The lower intensity of n–π* transitions was due to symmetry forbidden rules.[39,40,41]

Similar observations were made for ligand $\mathbf{L_2}$, having absorbance bands at 361 and 269 nm due to n–π* and π–π* transitions. For Fe(II)-$\mathbf{L_2}$-poly, the ligand band due to the n–π* transition disappeared similarly, indicating the complexation of the ligand with the metal ion. The d–d transition at 708 nm was observed for Fe(II)-$\mathbf{L_2}$-poly.

Fluorescence study

The fluorescence emission spectra of ligands $\mathbf{L_1}$ and $\mathbf{L_2}$ with their respective polymers are presented in Fig. 5. 10^{-5} M methanolic solutions of both ligands and their corresponding polymers were prepared for this study. All of these solutions were excited at 360 nm wavelength. The emission spectrum of ligand $\mathbf{L_1}$ showed a peak at 436 nm, which originates due to the transition from $S_1 \rightarrow S_0$.[42] In the case of ligand $\mathbf{L_2}$, an emission peak at 580 nm is observed.

In the solution state, Fe(II)-$\mathbf{L_1}$ has a strong emission peak at 440 nm, whereas Fe(II)-$\mathbf{L_2}$ exhibits a weak emission peak at 470 nm. Metal complexes possessing MLCT *via* the synergistic effect can exhibit higher intensity emission spectra than their corresponding ligand. At the same time, the metal-perturbed intra-ligand transitions (MPIL) cause a reduction of emission peaks in the coordination complex.[43–46] In the case of Fe(II)-$\mathbf{L_1}$, the MLCT predominates over MPIL, while Fe(II)-$\mathbf{L_2}$ has a weaker emission peak due to the predominance nature of MPIL over MLCT.

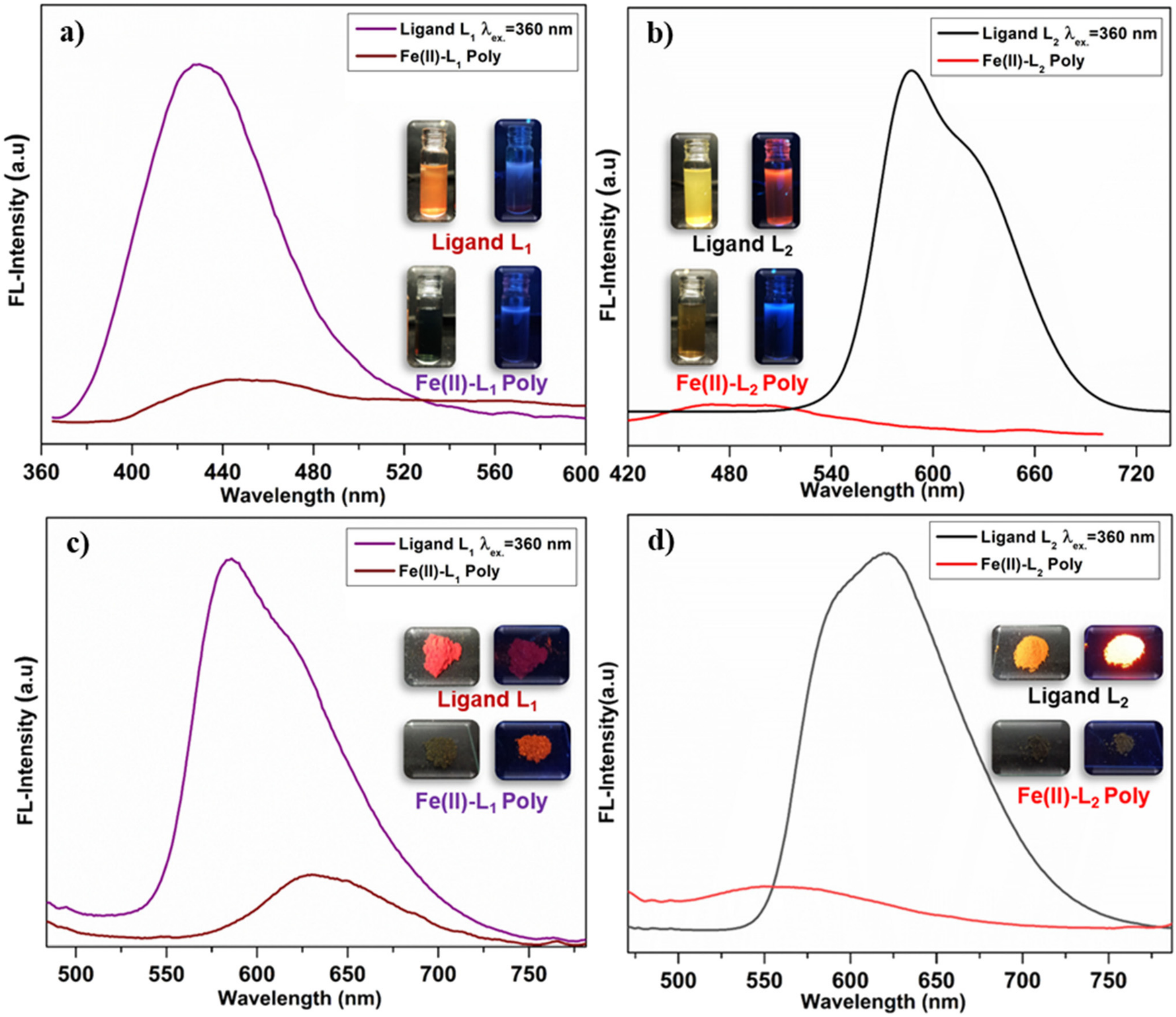

Fig. 5 Fluorescence spectra of (a) ligand $\mathbf{L_1}$ and Fe(II)-$\mathbf{L_1}$-poly at λ_{ex} 360 nm (in the solution state), (b) ligand $\mathbf{L_2}$ and Fe(II)-$\mathbf{L_2}$-poly at λ_{ex} 360 nm (in the solution state), (c) ligand $\mathbf{L_1}$ and Fe(II)-$\mathbf{L_1}$-poly at λ_{ex} 360 nm (in the solid state) and (d) ligand $\mathbf{L_2}$ and Fe(II)-$\mathbf{L_2}$-poly at λ_{ex} 360 nm (in the solid state).

On the other hand, for the solid-state fluorescence, the powdered samples of all four materials were subjected to 360 nm excitation. Ligand **L₁** did not show any solid-state fluorescence under bare-eye observation. Still, a weak emission peak was observed at 630 nm (*vide* Fig. 5c), an expected behaviour for many organic fluorophores due to the aggregation-caused quenching (ACQ) effect.[47] However, Fe(II)-$\mathbf{L_1}$-poly exhibits light orange fluorescence corresponding to 590 nm, which was absent in the liquid state. This is due to the metal–ligand charge transfer (MLCT) process. The reverse was observed for ligand $\mathbf{L_2}$ and its corresponding Fe(II)-$\mathbf{L_2}$ metallopolymer. For ligand $\mathbf{L_2}$, very bright orange fluorescence and the corresponding emission peak at 625 nm were observed, which showed a considerable decrease in the fluorescence intensity on complexation. Trivial positional isomerism triggers different types of packing of fluorophores in the two ligands in the solid state, and close packing of ligand $\mathbf{L_2}$ in the solid state was prevented, thus generating stable solid-state fluorescence.[47] We have observed a decrease in the fluorescence wavelength for the Fe(II)-$\mathbf{L_1}$ complex on moving from the solid state to the solution phase. The significant Stokes shift of the emission value in the solid state is due to the strong intermolecular interaction within the complexes. Our studies also match with the previously reported literature.[48–50]

Thermal studies

This analysis was done using DSC and TGA methods to determine the stability and thermal response of the two polymers. The thermogravimetric analysis results of Fe(II)-$\mathbf{L_1}$ and Fe(II)-$\mathbf{L_2}$-poly were recorded and are shown in Fig. 6. A two-step thermal degradation (as shown in DTG) was observed in the case of Fe(II)-$\mathbf{L_1}$-poly with approx. 30% mass loss initiated at a temperature of 280 °C, and then a sharp degradation with a mass loss of approximately 85% was observed up to 550 °C. In the case of Fe(II)-$\mathbf{L_2}$-poly, a three-step thermal degradation (as shown in DTG) was observed with approx. 20% mass loss initially up to a temperature of 221 °C followed by roughly 10% mass loss up to 292 °C. The third degradation was observed up to 560 °C with 85% mass loss. The second step degradation of Fe(II)-$\mathbf{L_2}$-poly confirms the chloride counter-ion satisfying the metal centre's primary valency, which correlates with the NMR, IR, counter-ion detection, and conductivity experiment results. The residue left in the case of Fe(II)-$\mathbf{L_1}$ and Fe(II)-$\mathbf{L_2}$-poly was about 15%, confirming the presence of metal oxides in the residue.

The DSC thermogram of Fe(II)-$\mathbf{L_1}$ and Fe(II)-$\mathbf{L_2}$-poly is shown in ESI Fig. S7 and S9,† respectively. For Fe(II)-$\mathbf{L_1}$ poly, the glass transition temperature (T_g) was observed at 140 °C, while for Fe(II)-$\mathbf{L_2}$ poly, T_g was observed at 125 °C. Both the polymers have semicrystalline characteristics; as a result, the crystalline temperature (T_c) for both polymers was observed at 210 °C and 230 °C. In the case of Fe(II)-$\mathbf{L_2}$ poly, T_c is more exothermic than that of Fe(II)-$\mathbf{L_1}$ poly. This might be possible because of the loss of HCl from Fe(II)-$\mathbf{L_2}$-poly. From the DSC thermograms, the melting points (T_m) of the crystalline zones were recorded at 265 °C and 280 °C for Fe(II)-$\mathbf{L_1}$ and Fe(II)-$\mathbf{L_2}$ poly, respectively.

Surface morphology

The morphologies of Fe(II)-$\mathbf{L_1}$-poly and Fe(II)-$\mathbf{L_2}$-poly were studied through AFM and FESEM techniques. For FESEM studies, both polymers were dissolved in DMSO : methanol (1 : 20) solution and a very dilute solution (10^{-5} M) was used for drop-casting on a Si wafer substrate (1 cm^2) for FESEM studies. The same solution was used for casting on a freshly cleaved, highly oriented pyrolytic graphite (HOPG) surface for AFM studies. However, it was injected from one corner of the HOPG substrate. With a sudden one-directional force, polymer chains present in a very dilute solution got detangled and aligned along the direction of the force. Both the substrates were dried under vacuum for 12 h. The AFM and FESEM images of Fe(II)-$\mathbf{L_1}$-poly are shown in Fig. 7a and b, respectively, and those of Fe(II)-$\mathbf{L_2}$-poly are shown in Fig. 8a and b, respectively.

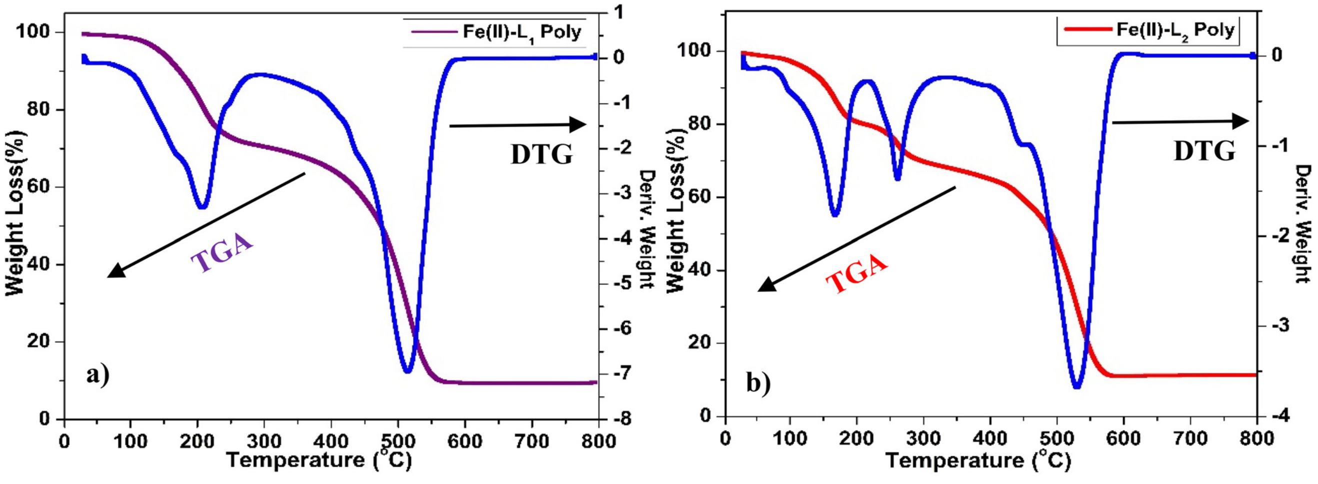

Fig. 6 (a) TGA-DTG thermogram of Fe(II)-$\mathbf{L_1}$-poly and (b) Fe(II)-$\mathbf{L_2}$-poly.

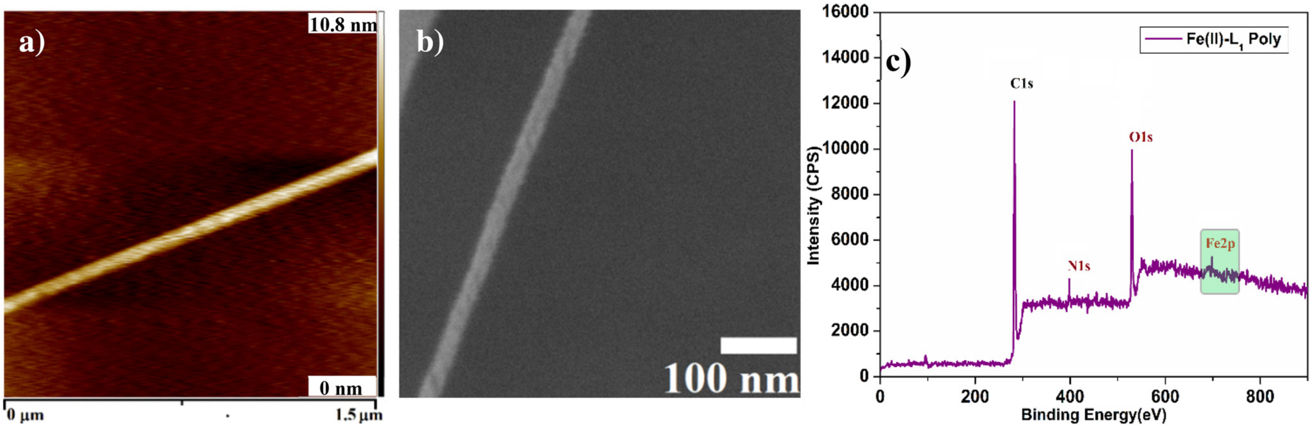

Fig. 7 (a) AFM images and (b) FESEM images of Fe(II)-L_1-poly on the HOPG substrate and Si wafer, respectively, and (c) XPS analysis of Fe(II)-L_1-poly.

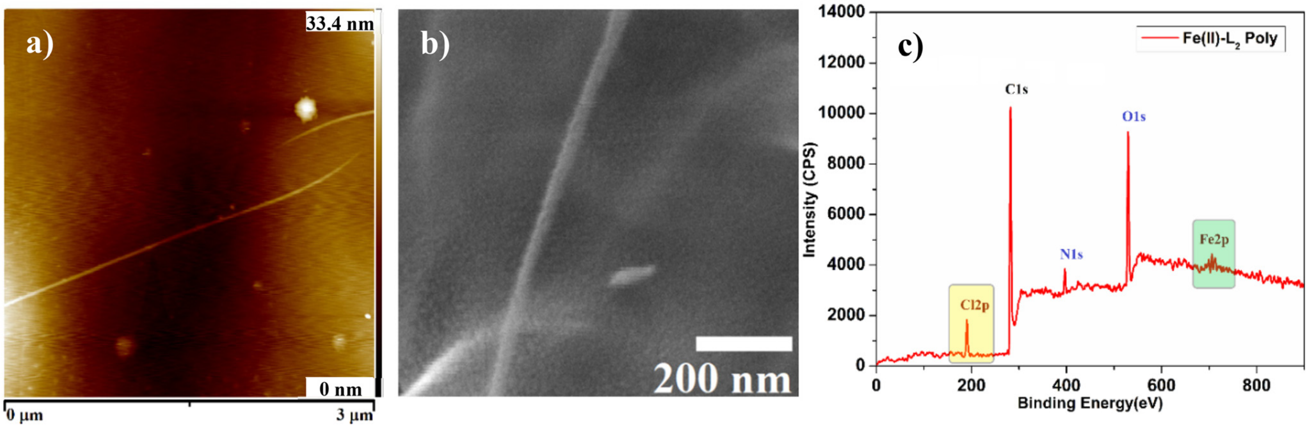

Fig. 8 (a) AFM images and (b) FESEM images of Fe(II)-L_2-poly on the HOPG substrate and Si wafer, respectively, and (c) XPS analysis of Fe(II)-L_2-poly.

This study's main objective was to understand the morphology of these metallopolymers for both Fe(II)-$\mathbf{L_1}$ and Fe(II)-$\mathbf{L_2}$-poly, and a long polymer nano-rod was observed in FESEM images. The thickness of the nano-rod formed by Fe(II)-$\mathbf{L_1}$-poly was 42 nm, while Fe(II)-$\mathbf{L_2}$-poly showed a thickness of 52 nm. The thickness of the nano-rod was measured using ImageJ software. The MM2 energy minimisation method of the octamer of similar polymers of Fe(II)-$\mathbf{L_1}$-poly and Fe(II)-$\mathbf{L_2}$-poly was carried out, and the thicknesses of individual polymer chains were found to be 2.62 and 3.01 nm, respectively. This confirmed that the obtained nano-rod of both polymers is an agglomeration of 15–17 individual polymer strands.

To confirm the proposed coordination pattern and oxidation state of iron, XPS analysis was done with both polymers,[51,52] and the spectra are presented in Fig. 7c and 8c for Fe(II)-$\mathbf{L_1}$ and Fe(II)-$\mathbf{L_2}$-poly, respectively. The presence of Cl^- ions is confirmed again in Fe(II)-$\mathbf{L_2}$-poly from its characteristic peak at 197.8 eV, as shown in Fig. 8c. This peak on further deconvolution (ESI Fig. S18e†) has been split into 197.25 eV and 199.15 eV, assigned to Cl $2p_{3/2}$ and Cl $2p_{1/2}$ peaks, respectively. The peak for Cl^- was absent in the Fe(II)-$\mathbf{L_1}$ spectrum. The peak obtained for the O 1s orbital in both polymers on deconvolution showed the combined contribution of C–O–Fe (530.2 eV) and O–Fe (529.8 eV) (*vide* ESI Fig. S18c†).

The Fe 2p peak at 709.6 eV upon deconvolution has been split into 708.9 eV for $2p_{3/2}$ and 723 eV for $2p_{1/2}$ peaks, which are Fe(II) ion characteristics. A shake-up satellite peak was observed at 715 eV for both polymers. So, the presence of central metal ions in the +2 oxidation state is confirmed by NMR and XPS analyses.

Electrochemical properties

The electrochemical behaviours of the ligands and their corresponding Fe(II) metallopolymers were studied using cyclic voltammetry (CV) experiments. A three-electrode electrochemical cell setup was employed with a glassy carbon as a working electrode, a Pt wire as the counter electrode, and Ag/AgCl as the reference electrode. The experiment was conducted in ACN solution containing 0.1 M TBAP as a supporting electrolyte at a scan rate of 100 mV s^{-1} under a nitrogen flow after removing all the dissolved oxygen by nitrogen purging for five minutes. The voltammograms obtained for the polymers are shown in Fig. 9 and 10, while those of the two ligands are pre-

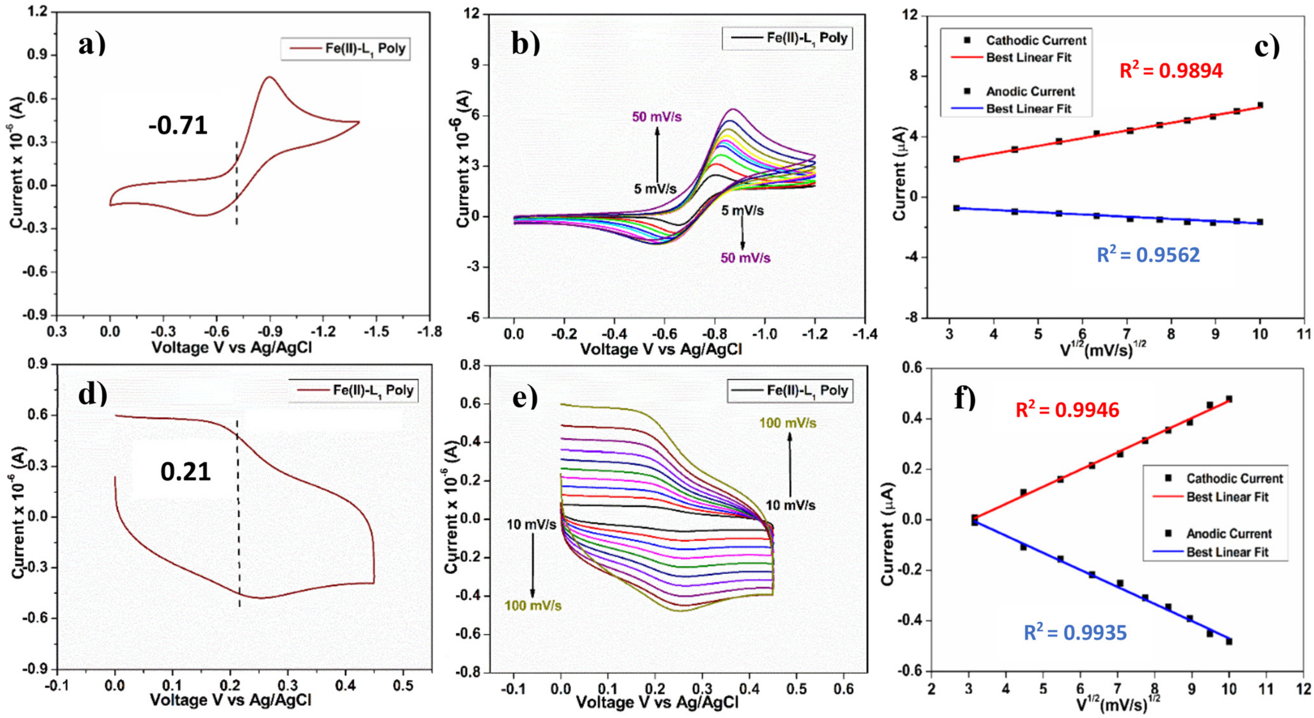

Fig. 9 Cyclic voltammogram of Fe(II)-L_1-poly (a) cathodic response, (b) cathodic response at a scan rate of 5–50 mV s^{-1}, (d) anodic response, (e) anodic response at a scan rate of 10–100 mV s^{-1} and (c and f) anodic (i_{pa}) and cathodic (i_{pc}) peak currents *vs.* square root of the scan rate ($V^{1/2}$).

sented in ESI, Fig. S10 and S11.† For ligand $\mathbf{L_1}$, one cathodic response was observed at −0.85 V, which was shifted to −0.71 V in the case of Fe(II)-$\mathbf{L_1}$-poly (*vide* Fig. 9a). This response was observed due to the reduction of the imine bond. Since the imine nitrogen of the ligand binds with the metal, a shift to the lower potential was observed upon coordination. None of the ligands exhibited any anodic response, as they do not get oxidised easily. On the other hand, metallopolymers possessing transition metal centres can be oxidised. This was also observed in the case of Fe(II)-$\mathbf{L_1}$-poly, which showed one anodic response at 0.21 V due to the oxidation couple of Fe(II)/Fe(III).

Similar observations were made in the case of ligand $\mathbf{L_2}$ and Fe(II)-$\mathbf{L_2}$-poly, in which the cathodic response of the ligand at −0.80 V was shifted to −0.69 V and an anodic response at 0.23 V was observed in the case of the polymer due to the oxidation of the Fe(II) state to the Fe(III) state.[15,51] To analyse the electron transfer mechanism during the redox process, CVs were measured at different scan speeds (5–100 mV s^{-1}) (Fig. 9 and 10 panels b and e, respectively). The anodic (i_{pa}) and cathodic (i_{pc}) peak currents in the redox process were plotted against the square root of the scan rate ($V^{1/2}$) (Fig. 9 & 10 panels c and f, respectively). The plots of i_{pa} or i_{pc} *vs.* $V_{1/2}$ were approximated by a straight line (the minimum mean square error (R^2): 0.99), indicating a reversible electron process through free diffusion of the active species.[52,54–56]

Spectroelectrochemical characterization

The metallopolymers' spectroelectrochemical study was conducted in the liquid state. The polymeric solutions of different concentrations were subjected to sequential potential change, and the results are shown in ESI Fig. S20.† The experiment was conducted using progressive potential application to the polymeric solutions, and the absorbance was monitored for 25 seconds after the application of the potential. The experiment was performed in a three-electrode cell consisting of a Ag wire as a reference electrode, a Pt-wire mesh as a working electrode, and a Pt wire as a counter electrode. All three electrodes were taken in a cuvette containing (polymer +0.1 M TBAP) in acetonitrile solution. After recording the ground state spectrum of the polymeric solutions, the potential was increased stepwise from 0 to 1.25 V with an increment of −0.25 V for each step. The optical changes were recorded using a UV-Vis spectrophotometer after each increment of applied potential. The spectral changes for Fe(II)-$\mathbf{L_1}$ and Fe(II)-$\mathbf{L_2}$-poly are shown in Fig. S20.†

For Fe(II)-$\mathbf{L_1}$-poly, a uniform increase in the absorption spectra with increasing potential was observed in the wavelength range of 350 nm to 460 nm. However, the spectral change observed when applying a potential to Fe(II)-$\mathbf{L_2}$-poly differed from that of Fe(II)-$\mathbf{L_1}$-poly. A uniform decrease in the absorption spectra with increasing potential was observed (Fig. S20b† showing a consistent decrease in the wavelength range from 350 nm to 450 nm with increasing potential from 0 to +1.25 V). Furthermore, the ground state absorbance was regenerated by applying the reverse potential in both cases. This helped to identify the reversible electrochemical behaviour of the polymer.

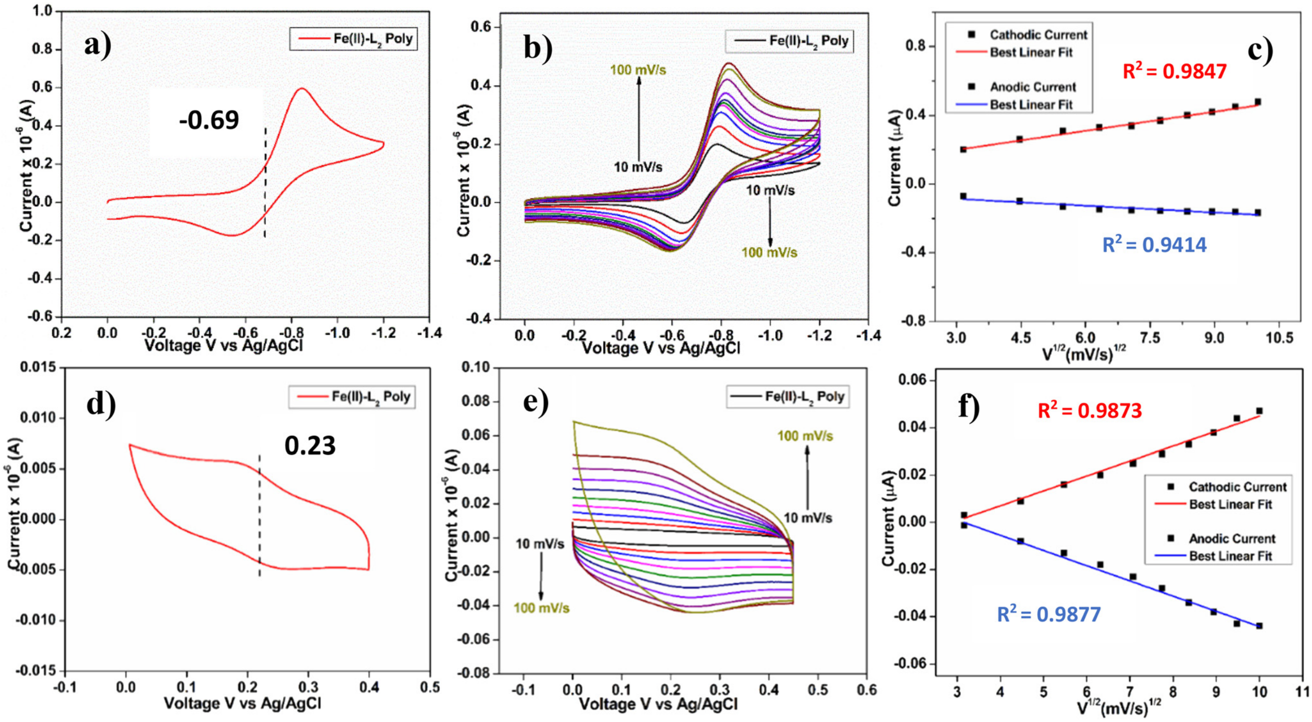

Fig. 10 Cyclic voltammogram of Fe(II)-L_2-poly (a) cathodic response, (b) cathodic response at a scan rate of 10–100 mV s^{-1}, (d) anodic response, (e) anodic response at a scan rate of 10–100 mV s^{-1} and (c and f) anodic (i_{pa}) and cathodic (i_{pc}) peak currents *vs.* square root of the scan rate ($V^{1/2}$).

Capacitance studies

The specific capacitance of the synthesised metal–ligand complex was measured through cyclic voltammetry in a three-electrode system, using the active material on 3 mm diameter GC as the working electrode, Ag/AgCl as the reference electrode, and a Pt wire as the counter electrode in 1 M LiCl aqueous solution. The working electrode was prepared using the drop-casting technique. After dissolving a certain amount of the metal–ligand complex in the DMSO solvent, a specific volume was drop-casted on GC, and then it was dried in an oven under vacuum for more than 24 h. The specific capacitance of Fe(II)-**L$_1$**-poly and Fe(II)-**L$_2$**-poly was found to be about 56 F g^{-1} and 41 F g^{-1} at 5 mV s^{-1} scan rates, respectively (Fig. 11a and d), which are comparable to the earlier reported Fe-metallopolymer.[57] The GCD experiments at current densities of 0.5, 1 and 2 A g^{-1} (*vide* Fig. 11b and e) were done, and experimental curves showed nearly linear discharge slopes and good symmetry. The specific capacitance at different current densities is shown in Fig. 11c and f. The cycling stability of Fe(II)-**L$_1$** and Fe(II)-**L$_2$**-poly at 1 A g^{-1} is shown in Fig. 11g and h for 50 cycles, while the experiment after 5000 charge–discharge cycles showed 98% retention of the initial capacitance for both (Fig. 11i and j). The potential was scanned from −1 V to 0.5 V. Specific capacitance was calculated from eqn (1).

$$C = A/(2 \times s \times m \times \Delta V) \quad (1)$$

where A = area under the curve, s = scan rate, m = mass of the active material and ΔV = potential window.

We have studied the effect of mass loading and scan rate on the capacitance value for both the metallopolymers (Fig. S21).† It is observed that with increasing scan rate, the specific capacitance is reduced for both metallopolymers. And, with increasing mass loading, the resistance value increased, negatively affecting the capacitance value. The CV graph shows that the oxidation peak shifts gradually towards a higher voltage, implying internal resistance. The intensity of the redox peak for ligand **L$_2$** is more than that of ligand **L$_1$**, suggesting that more redox reaction occurs in the case of ligand **L$_2$**.

Memristive studies

The surface morphology of the device was examined using AFM images, as shown in Fig. 12b. The AFM images were taken using a Park Systems XE-70 microscope in non-contact mode with a scan rate of 0.5 Hz, and the tip–sample distance was set to 10.5 nm throughout the measurement. Some pinholes (shown by green circles) are seen on the device surface. The average roughness of 41 nm has been obtained for the surface of the device.

I–V characterization

The current–voltage (*I–V*) characteristics of the device with Fe(II)-**L$_1$**-poly in a voltage range of −2 V to +2 V are shown in Fig. 13a. The *I–V* characteristics in the semi-log scale are shown in Fig. 13b. The current is low (10^{-6} A) up to +1.55 V, called the high resistance state (HRS) or OFF state. Further increment in the voltage on the positive side results in a sudden increase in the current in the range of 10^{-3} A, and the

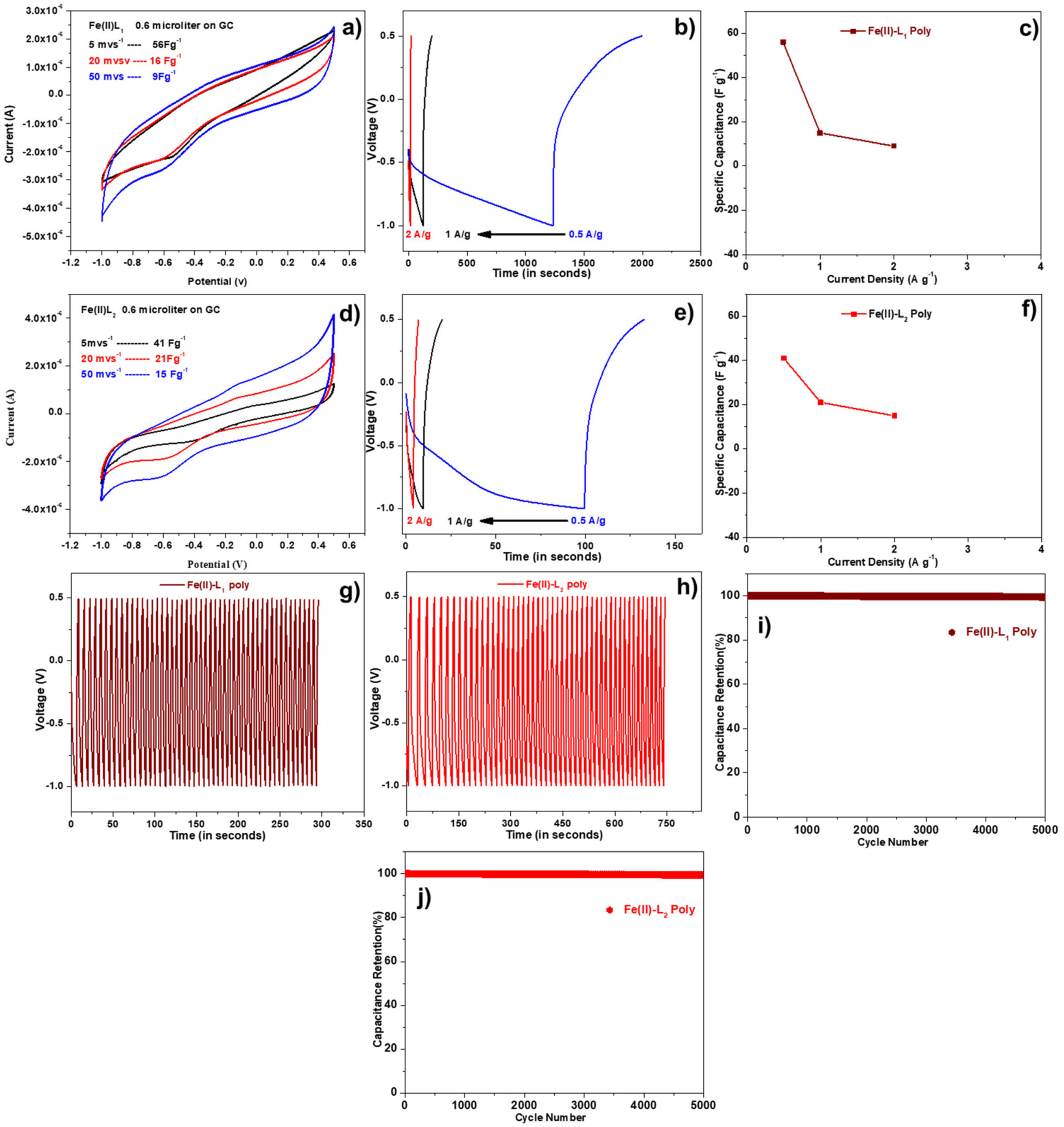

Fig. 11 Electrochemical performances of Fe(II)-L_1 and Fe(II)-L_2-poly in an aqueous LiCl electrolyte (a & d), CV curves at scan rates ranging from 0.05 to 1 mV s^{-1}, (b & e), GCD curves under various current densities (c & f), specific capacitance calculated at various current densities (g & h), and cycling stability tests at 1 A g^{-1} (i & j).

device goes from the high resistance state (HRS) to the low resistance state (LRS) or the ON state, which is called the SET operation of the device.[53,57,58] The device remains in the LRS at a voltage range of +1.55 V to +2 V, +2 V to 0 V, and even 0 V to −0.55 V. After a large negative voltage (−0.55 V), the current suddenly drops to 10^{-6} A and goes to the HRS again, which is called the RESET operation of the device. The device remains in the HRS at −0.55 to −2 V and −2 V to 0 V. This is the complete cycle of one total sweep from +2 V to −2 V. The HRS is assigned to 0 bit for the application of memory switching devices, and the LRS is assigned to 1 bit in logical operation. The maximum current ON–OFF ratio (I_{ON}/I_{OFF}) is 2 × 10^4 at 0.25 V for the device. To study the random access memory (RAM) characteristics of the device, successive voltage pulses

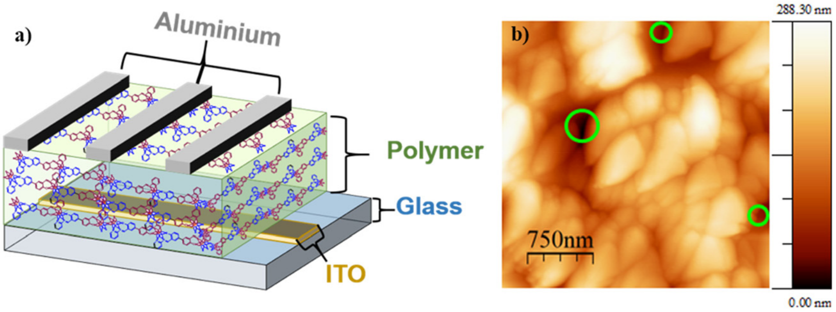

Fig. 12 (a) Schematic device structure for *I*–*V* characterisation and (b) AFM topography of the device where the green circles indicate pinholes on the surface.

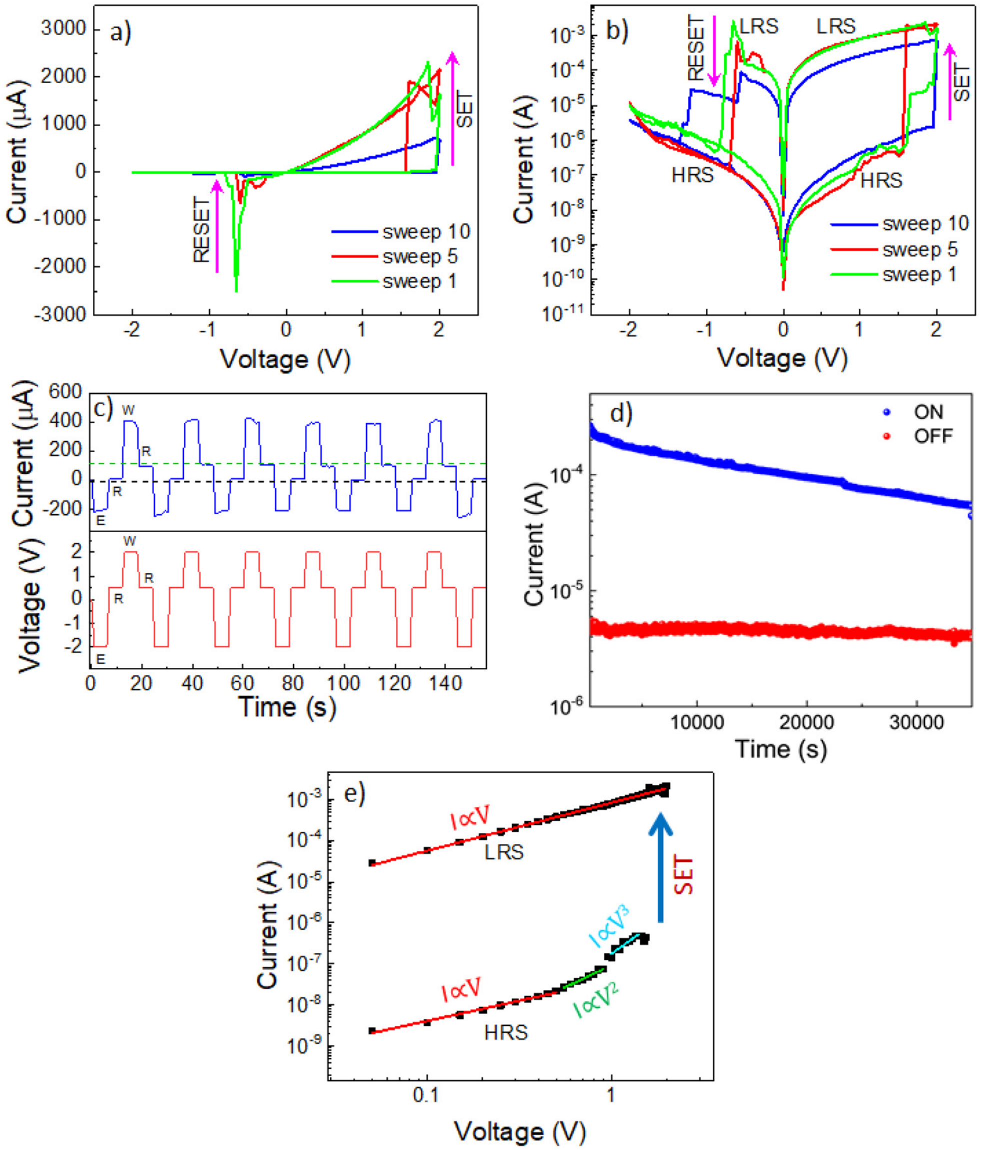

Fig. 13 *I*–*V* characteristic curves of the device from +2 V to −2 V with (a) linear scale, (b) semi-log scale, (c) "erase–read–write–read" studies where the green dashed line shows the ON current and the black dashed line shows the OFF current at a read voltage of 0.5 V, and (d) retention characteristic and (e) fitted log(*I*) *vs.* log(*V*) for a positive cycle where the LRS has only one region and the HRS has three distinct regions of conduction.

of −2 V (erase), +0.5 V (read), +2 V (write), and +0.5 V (read) with a pulse width of 6 s each were applied. The corresponding current values were recorded, as shown in Fig. 13c. A clear difference between ON and OFF currents at a read voltage of 0.5 V indicates good RAM behaviour. The retention test of the device was tested by applying a write, read and erase voltage of +2 V, +0.5 V, and −2 V, respectively, as shown in Fig. 13d. After using the write and erase pulse, the read current has a difference of greater than 10^1, which is maintained for longer than 35 000 seconds. We plotted the *I vs. V* curve in the log scale for the positive cycle to understand the conduction mechanism, as shown in Fig. 13e. There are three distinct regions in the HRS. At a low voltage (0 V to 0.5 V), the current varies linearly with the voltage ($I \propto V$), indicating the ohmic region. The current is low in this region because very few thermally excited carriers can participate in the conduction. According to Child's law, from 0.55 V to 0.9 V, the current varies as the square of the voltage ($I \propto V^2$), indicating trap-controlled space charge limited current (SCLC). From 0.95 V to 1.55 V, the $\log I$ *vs.* $\log V$ curve has a slope of 3 ($I \propto V^3$), which indicates trap-free SCLC conduction ($I \propto V^n$, $n > 2$).

At this point (1.55 V), all the trap states are filled by carriers, and conductive filaments form because of the penetration of metal atoms through the pinholes, as shown by green circles in the AFM topography of the device (Fig. 12b). After forming conductive filaments, the device goes from the HRS to the LRS (SET process). In the LRS state (2 V to 0 V), the $\log I$ *vs.* $\log V$ curve has a slope of 1, indicating that ohmic conduction and current are high due to the conducting filament formation. When a large negative voltage is applied, the filaments are ruptured, and the device goes from the LRS to the HRS again (RESET process). The devices made with both ligands did not show any memristive property. The memristive property of Fe(II)-**L₂** could not be measured as every attempt resulted in a short circuit in the device. This may be due to the higher intrinsic conductivity of the second polymer material, which was also observed in the solution state conductivity measurement.

Conclusion

In this research article, we have successfully synthesised and characterized two novel, multidentate, NNO donor ligands reported along with their metallopolymers. We aimed to understand the minimal tailorable change in the organic moiety (ligand), which could affect metallopolymers' properties. The current research has confirmed that a trivial change in the structure of ligands, like positional isomerism, can induce a drastic difference in the memristive property of metallopolymers. The first difference observed in these metallopolymers is their different coordination patterns, which was again confirmed through NMR, XPS and solution state conductivity studies. The second observation was the difference in the fluorescence properties of the synthesised ligands. The third remarkable difference was observed in the memristive properties in which the Fe(II)-**L₁** metallopolymer showed an outstanding (10^4) ON–OFF ratio and good ambient stability, while the Fe(II)-**L₂** metallopolymer showed a muted response. This positional isomerism also caused different solid-state fluorescence in the ligands. Ligand **L₂** showed bright orange fluorescence in the solid state, but ligand **L₁** did not, although all these ligands and polymers have good solution-state emission properties. These metallopolymers showed specific capacitance in the range of 50–60 F g^{-1} for Fe(II)-**L₁**-poly and 40–50 F g^{-1} for Fe(II)-**L₂** poly with 98% retention of the initial capacitance after 5000 charge–discharge cycles for both.

There is a search for an alternate, cheaper, non-volatile memristive material as the purification and fabrication of Si-based memristive devices are very costly. We can conclude that Fe(II)-**L₁**-poly has shown excellent potential to be used as a memristive material because of its robust ambient stability and good ON/OFF ratio.

Abbreviations

Ligand **L₁**	3,3′-Bis((*E*)-(pyridin-2-ylimino)methyl)-[1,1′-biphenyl]-4,4′-diol
Ligand **L₂**	3,3′-Bis((*E*)-(pyridin-3-ylimino)methyl)-[1,1′-biphenyl]-4,4′-diol

Author contributions

Shubham Bawa: investigation, formal analysis, experimental studies, visualization, data curation, writing – original draft, and revision of the manuscript and review, Anil Kumar: manuscript review, Gaurav Kumar Nim: experimental help, Prasenjit Kar: resources, manuscript review, and formatting of the manuscript, Jayanta Bera: memristive experimental help, Samaresh Ghosh: capacitance studies, Satyajit Sahu: memristive experimental help, manuscript review, and formatting of the manuscript, Anasuya Bandyopadhyay: conceptualization, methodology, resources, manuscript editing and review, revision of the manuscript, supervision, project administration, and funding acquisition.

Data availability

The data supporting this article have been included as part of the ESI.†

Conflicts of interest

There is no conflict of interest to declare.

Acknowledgements

S. Bawa is thankful to SERB, New Delhi, India, and Prof. Pradip. K. Maji, IITR. S. Bawa, G. Nim, and J. Bera thank the

MHRD, New Delhi, for their fellowship. A. K. is thankful to MHRD, New Delhi, and K.N University. S. G. acknowledges PMRF for the fellowship and funding (grant code – PM31-22-631-414). S. Bawa is also grateful to Dr. Tulika Sharma and Mr Vikas Kumar for their help and support.

References

1 D. Z. Zee, T. Chantarojsiri, J. R. Long and C. J. Chang, Metal-Polypyridyl Catalysts for Electro and Photochemical Reduction of Water to Hydrogen, *Acc. Chem. Res.*, 2015, **48**, 2027–2036.

2 P. C. Mondal, V. Singh and M. Zharnikov, Nanometric Assembly of Functional Terpyridyl Complexes on Transparent and Conductive Oxide Substrates: Structure, Properties, and Applications, *Acc. Chem. Res.*, 2017, **50**, 2128–2138.

3 J. F. Endicott, H. B. Schlegel, M. J. Uddin and D. S. Seniveratne, MLCT Excited States and Charge Delocalization in Some Ruthenium-Ammine-Polypyridyl Complexes, *Coord. Chem. Rev.*, 2002, **229**, 95–106.

4 A. El-ghayoury, A. Harriman, A. Khatyr and R. Ziessel, Controlling Electronic Communication in Ethynylated-Polypyridine Metal Complexes, *Angew. Chem., Int. Ed.*, 2000, **39**, 185–189.

5 A. E. Medlycott and G. S. Hanan, Synthesis and Properties of Mono and Oligo-Nuclear Ru(II) Complexes of Tridentate Ligands: The Quest for Long-Lived Excited States at Room Temperature, *Coord. Chem. Rev.*, 2006, **250**, 1763–1782.

6 D. A. Turchetti, A. J. Santana, L. G. T. A. Duarte, T. D. Z. Atvars, R. A. Domingues and L. Akcelrud, Ratiometric Thermochromism in Europium-Containing Conjugated Polymer, *Polymer*, 2019, **177**, 65–72.

7 P. Kiri, G. Hyett and R. Binions, Solid State Thermochromic Materials, *Adv. Mater. Lett.*, 2010, **1**, 86–105.

8 Y. Wang, E. L. Runnerstrom and D. J. Milliron, Switchable Materials for Smart Windows, *Annu. Rev. Chem. Biomol. Eng.*, 2016, **7**, 283–304.

9 M. X. Zhu, W. Lu, N. Zhu and C. M. Che, Structures and Solvatochromic Phosphorescence of Dicationic Terpyridyl-Platinum-(II) Complexes with Foldable Oligo (Ortho-Phenyleneethynylene) Bridging Ligands, *Chem. – Eur. J.*, 2008, **14**, 9736–9746.

10 M. Higuchi, Electrochromic Organic-Metallic Hybrid Polymers: Fundamentals and Device Applications, *Polym. J.*, 2009, **41**, 511–520.

11 A. Bandyopadhyay and M. Higuchi, From Metal Complexes to Metallosupramolecular Polymers Via Polycondensation: Synthesis, Structure and Electrochromic Properties of Co (III)- and Fe(III)-Based Metallosupramolecular Polymers With Aromatic Azo Ligands, *Eur. Polym. J.*, 2013, **49**, 1688–1697.

12 S. K. Deb, A Novel Electrophotographic System, *Appl. Opt.*, 1969, **8**, 192–195.

13 F. S. Han, M. Higuchi, Y. Akasaka, Y. Otsuka and D. G. Kurth, Preparation, Characterization, and Electrochromic Properties of Novel Co(II)-bis-2,2′:6′,2″-terpyridine Metallo-supramolecular polymers, *Thin Solid Films*, 2008, **516**, 2469–2473.

14 M. K. Bera, T. Mori, T. Yoshida, K. Ariga and M. Higuchi, Construction of Coordination Nanosheets Based on Tris (2,2′-Bipyridine)-Iron (Fe^{2+}) Complexes as Potential Electrochromic Materials, *ACS Appl. Mater. Interfaces*, 2019, **11**, 11893–11903.

15 A. Kumar, S. Bawa, K. Ganorkar, S. K. Ghosh and A. Bandyopadhyay, A. Synthesis and Characterization of Acid-Responsive Luminescent Fe(II) Metallopolymers of Rigid and Flexible Backbone N-Donor Multidentate Conjugated Ligands, *Inorg. Chem.*, 2020, **59**, 1746–1757.

16 V. K. Thakur, G. Ding, J. Ma, P. S. Lee and X. Lu, Hybrid Materials and Polymer Electrolytes for Electrochromic Device Applications, *Adv. Mater.*, 2012, **24**, 4071–4096.

17 Y. Wang, D. Astruc and A. S. Abd-El-Aziz, Metallopolymers for Advanced Sustainable Applications, *Chem. Soc. Rev.*, 2019, **48**, 558–636.

18 A. Bandyopadhyay, S. Sahu and M. Higuchi, Tuning of Nonvolatile Bipolar Memristive Switching in Co(III) Polymer with an Extended Azo Aromatic Ligand, *J. Am. Chem. Soc.*, 2011, **133**, 1168–1171.

19 S. Goswami, A. J. Matula, S. P. Rath, S. Hedstrom, S. Saha, M. Annamalai, D. Sengupta, A. Patra, S. Ghosh, H. Jani, S. Sarkar, M. R. Motapothula, C. A. Nijhuis, J. Martin, S. Goswami, V. S. Batista and T. Venkatesan, Robust Resistive Memory Devices Using Solution-Processable Metal-Coordinated Azo Aromatics, *Nat. Mater.*, 2017, **16**, 1216–1224.

20 D. Oberoi, P. Dagar, U. Shankar, G. Vyas, A. Kumar, S. Sahu and A. Bandyopadhyay, Design, Synthesis, and Characterization of a Fe(II)-polymer of a Redox non-innocent, Heteroatomic, Polydentate Schiff's Base Ligand: Negative Differential Resistance and Memory Behaviour, *New J. Chem.*, 2018, **42**, 19090–19100.

21 A. Wild, A. Winter, M. D. Hager and U. S. Schubert, Fluorometric Sensor Based on Bisterpyridine Metallopolymer: Detection of Cyanide and Phosphates in Water, *Analyst*, 2012, **137**, 2333–2337.

22 S. Halder, S. Garg and C. Chakraborty, Introducing Non-Conjugated Ionic Spacer in Metallo-Supramolecular Polymer: Generation of Nanofibers for High-Performance Electrochromic Supercapacitor, *Chem. Eng. J.*, 2023, 144361.

23 A. Bandyopadhyay and M. Higuchi, From Metal Complexes to Metallosupramolecular Polymers via Polycondensation: Synthesis, Structure and Electrochromic Properties of Co (III) and Fe(III) based Metallosupramolecular Polymers with Aromatic Azo Ligands, *Eur. Polym. J.*, 2013, **49**, 1688–1697.

24 D. Oberoi, P. Dagar, U. Shankar, S. Sahu and A. Bandyopadhyay, Stabilization of Pristine Low Resistive State in a Ruthenium(II)-Polymer of a Hexadentate Schiff

Base Ligand: Synthesis, Characterization, and Application as Nonvolatile Memory Device, *Eur. J. Inorg. Chem.*, 2020, 3048–3058.

25 M. K. Bera, Y. Ninomiya and M. Higuchi, Constructing Alternated Heterobimetallic [Fe(II)/Os(II)]Supramolecular Polymers with Diverse Solubility for FacileFabrication of Voltage-Tunable Multicolor Electrochromic Devices, *ACS Appl. Electron. Mater. Interfaces*, 2020, **12**, 14376–14385.

26 R. R. Koner, S. Sinha, S. Kumar, C. K. Nandi and S. K. Ghosh, 2-Aminopyridine derivative as fluorescence 'On–Off' molecular switch for selective detection of Fe^{3+}/Hg^{2+}, *Tetrahedron Lett.*, 2012, **53**, 2302–2307.

27 A. Kumar, S. Bawa and A. Bandyopadhyay, Design, Synthesis and Characterization of Novel Organic-Inorganic Hybrid Polymeric Materials for Electroluminescence Applications, *New J. Chem.*, 2020, **44**, 6709–6713.

28 A. Kumar, S. Bawa, K. Ganorkar, S. K. Ghosh and A. Bandyopadhyay, Synthesis, Characterization, Multi-Acid Fluorescence Sensing and Electroluminescence Properties of Cr(II) Based Polymers, *Polym. Chem.*, 2020, **11**, 6579–6590.

29 A. Winter and U. S. Schubert, Synthesis and Characterization of Metallo-Supramolecular Polymers, *Chem. Soc. Rev.*, 2016, **45**, 5311–5357.

30 G. R. Whittell, M. D. Hager, U. S. Schubert and I. Manners, Functional Soft Materials from Metallopolymers and Metallosupramolecular Polymers, *Nat. Mater.*, 2011, **10**, 176–188.

31 M. K. Bera, Y. Ninomiya and M. Higuchi, Stepwise Introduction of three different Transition Metals in Metallo-Supramolecular Polymer for Quad-Color Electrochromism, *Chem. Commun.*, 2021, **4**, 1–12.

32 C. Chakraborty, R. K. Pandey, M. D. Hossain, Z. Futera, S. Moriyama and M. Higuchi, Platinum(II)-Based Metallo-Supramolecular Polymer with Controlled Unidirectional Dipoles for Tunable Rectification, *ACS Appl. Mater. Interfaces*, 2015, **7**, 19034–19042.

33 M. W. Schneider, I. M. Oppel and M. Mastalerz, Exo–Functionalized Shape–Persistent [2 + 3] Cage Compounds: Influence of Molecular Rigidity on Formation and Permanent Porosity, *Chem. – Eur. J.*, 2012, **18**, 4156–4160.

34 D. Campbell, R. A. Pethrick and J. R. White, *Polymer Characterization: Physical Techniques*, CRC Press, New York, 2014.

35 B. J. Hunt and M. I. James, *Polymer Characterisation*, Chapman and Hall, Glasgow, 1993.

36 F. W. Billmeyer, *Textbook of Polymer Science*, Wiley, New York, 1994, reprint 2012.

37 C. E. Carraher, *Introduction to Polymer Chemistry*, Taylor & Francis, New York, 2017.

38 Zulkarnain, I. M. Khan, A. Afaq, M. Lal, A. Musheer and A. Nafe, Synthesis of Charge Transfer Complex of Chloranilic Acid as Acceptor with p-Nitroaniline as Donor: Crystallographic, UV-Visible Spectrophotometric and Antimicrobial Studies, *J. Mol. Struct.*, 2017, **1141**, 687–697.

39 E. Ergeçen, B. Ilyas, D. Mao, H. C. Po, M. B. Yilmaz, J. Kim, J. G. Park, T. Senthil and N. Gedik, Magnetically Brightened Dark Electron-Phonon Bound States in a van der Waals Antiferromagnet, *Nat. Commun.*, 2022, **13**, 1–7.

40 V. D. C. P. Barbosa, J. Xiong, P. M. Tran, M. A. McGuire, J. Yan, M. T. Warren, R. V. Aguilar, W. Zhang, M. Randeria, N. Trivedi, D. Haskel and P. M. Woodward, The Impact of Structural Distortions on the Magnetism of Double Perovskites Containing $5d^1$ Transition-Metal Ions, *Chem. Mater.*, 2022, **34**, 1098–1109.

41 H. M. Rhoda, A. J. Heyer, B. Snyder, D. Plessers, M. L. Bols, R. A. Schoonheydt, B. F. Sels and E. I. Solomon, Second-Sphere Lattice Effects in Copper and Iron Zeolite Catalysis, *Chem. Rev.*, 2022, **122**, 12207–12243.

42 S.-Y. Li, Z.-B. Sun and C.-H. Zhao, Charge-Transfer Emitting Triarylborane π-Electron Systems, *Inorg. Chem.*, 2017, **56**, 8705–8717.

43 A. O. Adeloye, Synthesis, Photophysical and Electrochemical Properties of a Mixed Bipyridyl-phenanthrolyl Ligand Ru(II) Heteroleptic Complex having trans-2-methyl-2-butenoic Acid Functionalities, *Molecules*, 2011, **10**, 8353–8367.

44 S. Ghosh, G. K. Nim, P. Bansal and P. Kar, Investigating the property of water driven lead-free stable inorganic halide double perovskites, *J. Colloid Interface Sci.*, 2021, **582**, 1223–1230.

45 G. K. Nim, P. Bansal and P. Kar, Nitrate ion-incorporated stable perovskite nanocrystals by a solvent-free mechanochemical reaction, *ACS Omega*, 2019, **4**, 15678–15683.

46 P. Bansal, Y. Khan, G. K. Nim and P. Kar, Surface modulation of solution processed Organolead halide perovskite quantum dots to large nanocrystals integrated with Silica gel G, *Chem. Commun.*, 2018, **54**, 3508–3511.

47 N. T. Harrison, D. R. Baigent, I. D. W. Samuel, R. H. Friend, A. C. Grimsdale, S. C. Moratti and A. B. Holmes, Site-selective fluorescence studies of poly (p-phenylene vinylene) and its derivatives, *Phys. Rev. B: Condens. Matter Mater. Phys.*, 1996, **53**, 15815–15822.

48 S. P. Anthony, Organic solid–state fluorescence: strategies for generating switchable and tunable fluorescent materials, *ChemPlusChem*, 2012, 518–531.

49 B. Shao, M. Baroncini, H. Qian, L. Bussotti, M. Di Donato, A. Credi and I. Aprahamian, Solution and solid-state emission toggling of a photochromic hydrazone, *J. Am. Chem. Soc.*, 2018, **140**, 12323–12327.

50 H. C. Wu, P. Thanasekaran, C. H. Tsai, J. Y. Wu, S. M. Huang, Y. S. Wen and K. L. Lu, Self-assembly, reorganization, and photophysical properties of Silver(I)–schiff-base molecular rectangle and polymeric array species, *Inorg. Chem.*, 2006, **45**, 295–303.

51 Y. S. L. V. Narayana, S. Mondal, U. Rana, Y. Ninomiya, D. C. Santra, T. Yoshida and M. Higuchi, One-Step Synthesis of a Three-Dimensionally Hyperbranched Fe(II)-Based Metallo-Supramolecular Polymer Using an Asymmetrical Ditopic Ligand for Durable Electrochromic Films with Wide Absorption, Large Optical Contrast, and

High Coloration Efficiency, *ACS Appl. Electron. Mater.*, 2021, **3**(5), 2044–2055.

52 D. C. Santra, S. Mondal, T. Yoshida, Y. Ninomiya and M. Higuchi, Ru(II)-Based Metallo-Supramolecular Polymer with Tetrakis(N-methylbenzimidazolyl)bipyridine for a Durable, Nonvolatile, and Electrochromic Device Driven at 0.6 V, *ACS Appl. Electron. Mater. Interfaces*, 2021, **13**(26), 31153–31162.

53 D. Oberoi, P. Dagar, U. Shankar, G. Vyas, A. Kumar, S. Sahu and A. Bandyopadhyay, Differential Resistance and Memory Behaviour, *New J. Chem.*, 2018, **42**, 19090–19100.

54 S. Napierala, M. Kubicki and M. Chorab, Toward Electrochromic Metallopolymers: Synthesis and Properties of Polyazomethines Based on Complexes of Transition-Metal Ions, *Inorg. Chem.*, 2021, **60**(18), 14011–14021.

55 R. S. Assary, F. R. Brushett and L. A. Curtiss, Reduction Potential Predictions of some Aromatic Nitrogen-Containing Molecules, *RSC Adv.*, 2014, **4**, 57442–57451.

56 W. Kaim, Chelate rings of different sizes with non-innocent ligands, *Dalton Trans.*, 2019, **48**, 8521–8529.

57 R. R. Pradhan, J. Bera, A. Betal, P. Dagar and S. Sahu, Hot injection-based synthesized colloidal CdSe quantum dots embedded in Poly (4-vinylpyridine)(PVP) matrix form a nanoscale heterostructure for a high on–off ratio memory-switching device, *ACS Appl. Mater. Interfaces*, 2021, **13**(21), 25064–25071.

58 A. Betal, J. Bera, A. Sharma, A. K. Rath and S. Sahu, Composition and surface morphology invariant high On–Off Ratio from an organic memristor, *ACS Appl. Electron. Mater.*, 2022, **4**, 1109–1116.